Computer Methods in Applied Mechanics and Engineering 418 (2024) 116521

Contents lists available at ScienceDirect

Comput. Methods Appl. Mech. Engrg.

journal homepage: www.elsevier.com/locate/cma

A Bayesian defect-based physics-guided neural network model for probabilistic fatigue endurance limit evaluation

Alessandro Tognan [a,*], Andrea Patanè [b], Luca Laurenti [c], Enrico Salvati [a]

[a] Polytechnic Department of Engineering and Architecture, University of Udine, Via delle Scienze 206, Udine, 33100, Italy
[b] Trinity College Dublin, The University of Dublin, College Green, Dublin, 2, Ireland
[c] Delft Centre of System and Control (DCSC), TU Delft University, Mekelweg 2, Delft, 2628, The Netherlands

ARTICLE INFO

Keywords:
Fatigue strength
Defects
Bayesian Physics-guided Neural Networks
Uncertainty quantification
Additive manufacturing

ABSTRACT

Accurate fatigue assessment of material plagued by defects is of utmost importance to guarantee safety and service continuity in engineering components. This study shows how state-of-the-art semi-empirical models can be endowed with additional defect descriptors to probabilistically predict the occurrence of fatigue failures by exploiting advanced Bayesian Physics-guided Neural Network (B-PGNN) approaches. A B-PGNN is thereby developed to predict the fatigue failure probability of a sample containing defects, referred to a given fatigue endurance limit.

In this framework, a robustly calibrated El Haddad's curve is exploited as the prior physics reinforcement of the probabilistic model, i.e., prior knowledge. Following, a likelihood function is built and the B-PGNN is trained via Bayesian Inference, thus calculating the posterior of the parameters. The arbitrariness of the choice of the related architecture is circumvented through a Bayesian model selection strategy. A case-study is analysed to prove the robustness of the proposed approach. This methodology proposes an advanced practical approach to help support the probabilistic design against fatigue failure.

1. Introduction

Defects broadly embody diverse unintended material features that originate from any fabrication process, encompassing casting, welding, sintering and additive manufacturing (AM) [1–3]. Although limitedly employed in practical engineering problems, a great deal of scientific interest has recognised material defects as the foremost cause of fatigue collapse. Specifically, defects induce local stress concentrations interfering with in-service fatigue loads and thus promoting fatigue crack initiation. Moreover, these phenomena are highly sensitive to defect's shape and location with respect to the free-surface of the considered structural components [4–6].

Although numerous post-fabrication treatments aim to mitigate material defectivity, its presence appears inescapable in some instances [7–9]. Therefore, defect-based models ought to be pursued for designing mechanical components against fatigue failure [10]. When defects can be regarded as cracks, their impact on fatigue performance can be assessed exploiting Fracture Mechanics (FM). Provided a representative characteristic length for such crack-like defects, several semi-empirical fatigue crack growth models are available to assess the fatigue life as well as the fatigue endurance limit of metallic materials, e.g. Paris', Murakami's, and El Haddad's (EH) [11–13]. For decades, these fatigue semi-empirical models have constituted the mainstream for designing metallic parts against fatigue failure [14,15]. Despite their practicality, such models are not capable to fully consider

* Corresponding author.
E-mail addresses: tognan.alessandro@spes.uniud.it (A. Tognan), apatane@tcd.ie (A. Patanè), L.Laurenti@tudelft.nl (L. Laurenti), enrico.salvati@uniud.it (E. Salvati).

https://doi.org/10.1016/j.cma.2023.116521
Received 4 August 2023; Received in revised form 14 September 2023; Accepted 5 October 2023
Available online 14 October 2023

the real morphology of defects; generally highly complex. On top of that, other material inhomogeneities present at the micron- and sub-micron-scale are completely neglected in current predictive models, such as residual stress (RS) and intrinsic material fatigue strength. These shortcomings reveal the limitations of such semi-empirical models. As far as the defect morphology is concerned, the leading trend in characterising materials is seeing the use of both computed tomography (CT) and post-mortem fractography, to thoroughly acquire relevant descriptors of defects, thus enriching their characterisation – particularly in the context of AM [3,16–20]. Nevertheless, the current use of this powerful technique is only exploited partially given that, FM models cannot handle defect features other than the representative length.

To tackle this caveat, Machine Learning (ML) approaches have recently gained popularity to achieve superior defect-based assessment of fatigue performance [21–23]. To this end, a wealth of application of ML algorithm can be found in the literature regarding diverse metallic alloys, e.g. Neural Networks (NN) [24–29], Random Forest [28–30], Support Vector Machines [28,29,31–33], Kernel Ridge Regression [33,34], Gaussian Process Regression [29]. Due to the pure data-driven training of these ML approaches and due to the generally scarce available experimental data, the resulting surrogate models might recognise biased data patterns and lead to predictions not complying with the observed phenomenon. This drawback has recently fostered the development of Physics Informed Neural Networks (PINNs), whose training is constrained by physical or phenomenological laws [35,36]. Although PINNs were originally developed to numerically solve partial differential equations (PDEs), their rationale has been transferred to deal with problems related to fatigue life assessment. A few authors of the present manuscript conceived a defect-based PINN reinforced by a linear elastic FM (LEFM) model to correlate a set of defect descriptors with the fatigue life of a batch of AlSi10Mg specimens [37,38].

Reportedly, defects cause scattered fatigue data which, consequently, retain both epistemic and aleatory uncertainty [39–42]. Therefore, deterministic and frequentist data-driven and physics informed ML models cannot adequately account this aspect that is of great importance when designing engineering components against fatigue failure. Moreover, this approaches may suffer from small-data regimes. For this reason, the employment of probabilistic approaches is gaining more interest. Instead, Bayesian Inference (BI) represents a neat solution to address this problem which provides a formal probabilistic modelling setting with a built-in uncertainty quantification framework, provided adequate prior domain knowledge [43–45]. These methods inherit from BI the ability to craft surrogate models whose complexity is linked with the nature of the problem while minimising the dependence on the data regime [46]. Despite this, relatively little research has been devoted to applying formal BI-based methods to fatigue-related problems [40,47–49]. Given the potential of the Bayesian setting, BI and NNs have elegantly been blended, thus defining a new paradigm of ML, namely Bayesian NNs (BNNs) [46,50–52]. Thanks to BI, BNNs demonstrates excellent predictive capabilities in the context of small datasets [53], even when the number of samples is lower than the dimensionality of the problem [54]. More recently, the realm of BNNs has witnessed the advent of Bayesian PINNs (B-PINNs) [55]. Although primarily focused on PDE-governed problems [56–58], B-PINNs efficiently combines the distinctive capabilities of PINNs with BI. Hence, B-PINNs apparently represent a powerful probabilistic ML tool to address the evaluation of fatigue performance, while embedding appropriate phenomenological laws into the training and offering a formal uncertainty quantification framework.

The present manuscript borrows part of the B-PINN's framework to conceive a B-PGNN that predicts whether a specimen retaining certain defectivity traits attains a given fatigue life, i.e. number of cycles, when subjected to a prescribed fatigue load; sometimes referred to as material fatigue limit. The present investigation concentrates on an Selective Laser Melted (SLM) AlSi10Mg literature dataset whose specimens were tested via alternate tensile fatigue tests. Comprehensive defect descriptors are available from both ante- and post-mortem analysis via CT-scan and fractography, respectively. Initially, the fractographic data and further literature information are used to determine the EH defect sensitivity curve of the dataset following Ref. [49]. The retrieved EH curve is then opportunely generalised to handle the descriptors contained in the CT-dataset. The generalised EH curve is then transferred to the parameters (weights & biases) of the B-PGNN as a prior (distribution) to inform its physical side. Whilst the data-driven side of the B-PGNN is ruled by the likelihood (function) built upon the available experimental CT dataset. Thus, BI is pursued to compute the posterior (distribution) of the parameters. Consequently, the B-PGNN learns how to predicts the failure probability of the samples while providing the uncertainty of such predictions. Furthermore, a K-fold cross-validation is performed to assess the robustness of the B-PGNN, and its performance over the BNN counterpart are examined. Alongside, a Bayesian model selection method is presented to identify the optimal B-PGNN architecture amongst many candidate configurations. As an ancillary result, the B-PGNN is exploited to shed light onto the correlations between the predictions and descriptors from CT-scans, which would not be disclosed if the classic EH model were adopted.

2. Bayesian Physics Guided Neural Networks

For an input point $\mathbf{x} \in \mathbb{R}^n$, let $\mathcal{F}$ a feed-forward NN with $l = 1, 2, \dots, L$ fully-connected layers having $N_1, N_2, \dots, N_l$ neurons each. Inductively, $\mathcal{F}$ is defined over the number of layers as follows:

$$\mathbf{y}_1(\mathbf{x}) = \mathbf{W}_1\mathbf{x} + \mathbf{b}_1, \tag{1}$$

$$\mathbf{y}_l(\mathbf{x}) = \mathbf{W}_l\,\varphi(\mathbf{y}_{l-1}(\mathbf{x})) + \mathbf{b}_l, \quad l = 2, \dots, L \tag{2}$$

$$\mathcal{F}(\mathbf{x}) = \mathbf{y}_L(\mathbf{x}) \tag{3}$$

where φ represents the activation function. As concerns the l-th, $\mathbf{W}_l$ and $\mathbf{b}_l$ are weight matrix and bias vector thereof. Whilst N_l denotes the number of neurons of the l-th layer. Henceforth, $\boldsymbol{\theta}$ will denote the aggregated vector of weights and biases.

Let D be a dataset generated by an underlying ground-truth function one wish to learn. Bayesian modelling aims to assimilate the function by capturing the uncertainty in the learning process [59] – it does so by turning model parameters (i.e. weights & biases

in the case of NNs) into random variables. In particular, Bayesian modelling commences with placing a *prior* over the network parameters $\mathbb{P}[\boldsymbol{\theta}|\mathcal{F}]$. Intuitively, the prior represents the previous knowledge of the modeller about the observed phenomenon. The fit of the network $\mathcal{F}$ to the data $\mathcal{D}$ is assessed through the *likelihood* $\mathbb{P}[\mathcal{D}|\boldsymbol{\theta},\mathcal{F}]$ [60]. BI then combines the likelihood and prior via Bayes's theorem to obtain the *posterior* over the NN parameters:

$$\mathbb{P}[\boldsymbol{\theta}|\mathcal{D},\mathcal{F}] = \frac{\mathbb{P}[\mathcal{D}|\boldsymbol{\theta},\mathcal{F}]\,\mathbb{P}[\boldsymbol{\theta}|\mathcal{F}]}{\mathbb{P}[\mathcal{D}|\mathcal{F}]} \tag{4}$$

where $\mathbb{P}[\mathcal{D}|\mathcal{F}]$ is called the *model evidence* defined as:

$$\mathbb{P}[\mathcal{D}|\mathcal{F}] = \int_{\boldsymbol{\theta}} \mathbb{P}[\mathcal{D}|\boldsymbol{\theta},\mathcal{F}]\,\mathbb{P}[\boldsymbol{\theta}|\mathcal{F}]\,d\boldsymbol{\theta}. \tag{5}$$

Once the posterior distribution is computed, one can draw $\boldsymbol{\theta}^{(j)}\ j = 1,\dots,\mathsf{N}$ trials from it and perform predictions $\mathcal{F}(\mathbf{x}_*) = \mathcal{F}_*$ on an unseen input $\mathbf{x}_*$ by computing the *predictive posterior* (distribution):

$$\mathcal{F}_* = \mathbb{P}[\mathbf{x}_*|\mathcal{D},\mathcal{F}] \approx \frac{1}{\mathsf{N}}\sum_{j=1}^{\mathsf{N}} \mathbb{P}[\mathbf{x}_*|\boldsymbol{\theta}^{(j)},\mathcal{F}]. \tag{6}$$

Upon determining $\mathbb{P}[\mathbf{x}_*|\mathcal{D},\mathcal{F}]$, one can draw a sufficient number of trials $\mathcal{F}_*^{(k)}\ \forall\, k = 1,2,\dots,\mathsf{P}$ whereby pertinent statistical indicators can be computed accordingly, such as the expected value (mean) $\mathbb{E}[\mathcal{F}_*]$, standard deviation (uncertainty) $\sqrt{\mathbb{V}[\mathcal{F}_*]}$. Additionally, one can compute the 2.5% and 97.5% quartiles, and the 25% and 75% quartiles to calculate the 95% confidence interval and the interquartile range of $\mathbb{P}[\mathbf{x}_*|\mathcal{D},\mathcal{F}]$, respectively.

Unfortunately, for NNs the exact computation of Eq. (4) is generally unfeasible. Consequently, the computation of $\mathbb{P}[\boldsymbol{\theta}|\mathcal{D},\mathcal{F}]$ requires approximations, and approximate BI methods such as Hamiltonian Monte Carlo (HMC) [46,61] and Variational Inference (VI) [62–65] are generally employed. As both methods are used in the present manuscript, their brief summary is given herein.

HMC defines a set of Markov chains whose invariant distribution is $\mathbb{P}[\boldsymbol{\theta}|\mathcal{D},\mathcal{F}]$ and relies on Hamiltonian dynamics to accelerate the exploration of the distribution space. Because the invariant distribution of the Markov chains is $\mathbb{P}[\boldsymbol{\theta}|\mathcal{D},\mathcal{F}]$, the training performed with HMC is guaranteed to converge asymptotically to the exact posterior distribution.

VI defines an approximating posterior distribution $\mathbb{Q}_{\boldsymbol{\lambda}}(\boldsymbol{\theta}) \approx \mathbb{P}[\boldsymbol{\theta}|\mathcal{D},\mathcal{F}]$ from a given class, e.g., Gaussian. VI assumes that $\mathbb{Q}_{\boldsymbol{\lambda}}(\boldsymbol{\theta})$ depends on the parameters in $\boldsymbol{\lambda}$ which are selected in order to minimise a distance between $\mathbb{Q}_{\boldsymbol{\lambda}}(\boldsymbol{\theta})$ and the true posterior and, consequently, to find the closest $\mathbb{Q}_{\boldsymbol{\lambda}}(\boldsymbol{\theta})$ to $\mathbb{P}[\boldsymbol{\theta}|\mathcal{D},\mathcal{F}]$ within the given class. Whilst VI has no convergence guarantees with respect to the true posterior, it often holds advantages in terms of computational complexity.

The B-PGNN conceived herein is essentially a NN trained through BI, i.e. by employing Eq. (4) In particular, the physical laws governing the observed phenomenon is embedded in the prior $\mathbb{P}[\boldsymbol{\theta}|\mathcal{F}]$, whereas the likelihood is generally assumed to be Gaussian in a regression setting, or Multinoulli in a classification setting [60]. The training scheme of the B-PGNN is illustrated in Fig. 1, whilst the details about designing the prior to include the physical law shall be discussed in Section 3.3 with particular regard to *catalytic priors* [66,67].

It is worth mentioning that the B-PINN framework has already been presented in [55]. Therein, the physics governing the problem is injected as to modify the likelihood, instead of the prior distribution. It is important to remark that one approach does not exclude the other. However, while the likelihood modification approach is more akin to the training for deterministic PINNs, designing priors tailored at a particular application is the natural channel for embedding expert knowledge in BNNs [46,67,68]. Crucially, crafting priors resembling the problem's formulation is an essential requirement to obtain good quality uncertainty estimation and a well-calibrated posterior [69].

3. Materials and methods

3.1. Material dataset

The present study considers as a case study the literature dataset borrowed from [17]. In particular, this dataset regards a batch of n.12 SLM AlSi10Mg specimens encompassing their fatigue characterisation, ante-mortem CT defectivity assessment, and post-mortem failure analysis. The specimens were turned after their fabrication to reduce their surface roughness, but no thermo-mechanical treatments were applied to relieve RS or mitigate defectivity.

The fatigue response of the samples was probed employing a cyclic load with constant stress amplitude $\Delta\sigma$ at load ratio $R = -1$. The recorded fatigue life N of each specimen as well as the corresponding applied stress range are listed in Table 1. The runout threshold $\mathcal{T} = 2\cdot 10^6$ was set to distinguish samples as either runout or failed, i.e. $N \geq \mathcal{T}$ and $N < \mathcal{T}$, respectively.

Before fatigue testing, each specimen were examined through CT to characterise its defectivity. Specifically, CT-scans enabled the retrieval of the external area, A, and the volume, V, of the detected defects whereby additional morphological features were derived. The projection of A onto the plane normal to the applied fatigue load provides the associated Murakami's parameter $\sqrt{\text{area}}$ [12]. Furthermore, the combination of both A and V lead to the so-called sphericity S:

$$S = \frac{\pi^{1/3}\,(6V)^{2/3}}{A} \tag{7}$$

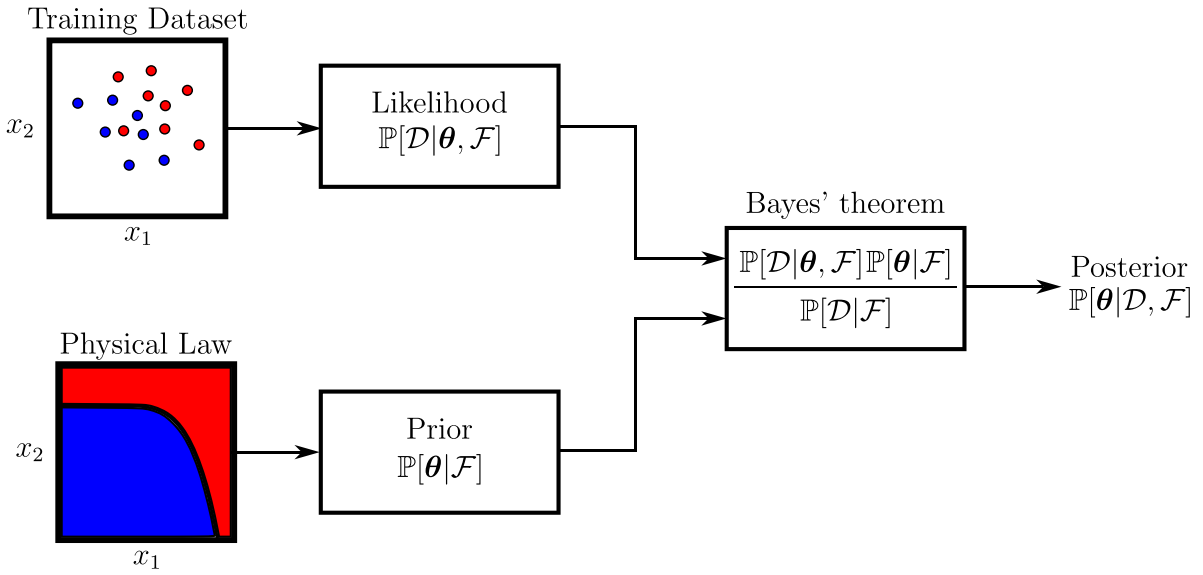

Fig. 1. Block diagram of the training the B-PGNNs $\mathcal{F}$. The prior distribution of the parameters $\boldsymbol{\theta}$, i.e. $\mathbb{P}[\boldsymbol{\theta}|\mathcal{F}]$, is inferred from a "physical" law. Given a training dataset $\mathcal{D}$ the likelihood $\mathbb{P}[\mathcal{D},|\boldsymbol{\theta},\mathcal{F}]$ is built, which is plugged along with the prior into Bayes's theorem. As a result the posterior $\mathbb{P}[\boldsymbol{\theta}|\mathcal{D},\mathcal{F}]$ is computed, alternatively through VI or HMC, allowing for subsequent predictions.

Table 1
Summary of the fatigue test campaign. Samples marked with $*$ underwent prior testing at a lower $\Delta\sigma$.

Sample	$\Delta\sigma$ [MPa]	N [–]	Outcome
1	295.4	46255	Failed
2	400.0	474	Failed
3	220.0	8889311	Runout
3*	360.0	3432	Failed
4	156.0	3795336	Runout
5	301.6	39538	Failed
6	378.3	11465	Failed
7	298.5	19806	Failed
8	156.0	20000000	Runout
9	180.0	11352768	Runout
10	220.0	2622640	Runout
11	180.0	237485	Failed
12	200.0	15242310	Runout

whereas, the sole V permits computing the equivalent diameter d:

$$d = \sqrt[3]{\frac{6V}{\pi}} \tag{8}$$

Whilst the position of the defects, h, was quantified by estimating the relative distance between their centroid and the free-surface of the examined specimen.

Postulating crack-like defect approximation, LEFM enables mode I SIF range ΔK to be assumed as the fatigue crack driving force. In this instance, $\sqrt{\text{area}}$ is adopted as the representative length of defects whereby ΔK is formulated as [70]:

$$\Delta K = Y \Delta\sigma \sqrt{\pi \sqrt{\text{area}}} \tag{9}$$

where the factor Y is evaluated according to Murakami's criterion [70]:

$$Y = \begin{cases} 0.65 & h/r < 1.25 \\ 0.5 & h/r \geq 1.25 \end{cases} \tag{10}$$

in which $r = \sqrt{\text{area}/\pi}$ is the equivalent radius of the defect. Amongst numerous acquired defects for each sample, the present research prioritises those yielding the maximum ΔK, see Table 2.

Post-mortem fractography characterised, where detectable, the defects that actually triggered fatigue failure in terms of $\sqrt{\text{area}}$ and, again, the distance h between the defect's centroid and the free-surface of the specimen. Additionally, Murakami's criterion

Table 2
Defect descriptors acquired via CT-scan yielding the maximum ΔK.

Sample	$\sqrt{\text{area}}$ [µm]	h [µm]	d [–]	S [–]	Y [–]	ΔK [MPa$\sqrt{\text{m}}$]
1	214.2	110.9	186.7	0.35	0.65	5.0
2	275.0	308.8	256.5	0.27	0.65	7.6
3	283.4	134.3	253.0	0.25	0.65	4.3
4	334.5	233.8	227.6	0.32	0.65	3.3
5	379.1	269.5	260.9	0.29	0.65	6.8
6	429.2	222.8	340.6	0.23	0.65	9.0
7	443.3	207.6	401.8	0.21	0.65	7.2
8	458.2	214.2	341.4	0.24	0.65	3.8
9	470.0	222.3	342.6	0.25	0.65	4.5
10	497.8	310.1	418.3	0.17	0.65	5.7
11	568.8	332.0	398.6	0.20	0.65	4.9
12	572.0	373.7	410.2	0.21	0.65	5.5

Table 3
Available defect descriptors acquired via fractography.

Sample	$\sqrt{\text{area}}$ [µm]	Y [–]	ΔK [MPa$\sqrt{\text{m}}$]
1	128.8	0.65	3.9
2	378.2	0.65	9.0
3	168.8	0.65	5.4
8	500.0	0.65	2.6
9	437.4	0.65	4.3
10	271.5	0.65	4.2
12	440.0	0.65	4.2

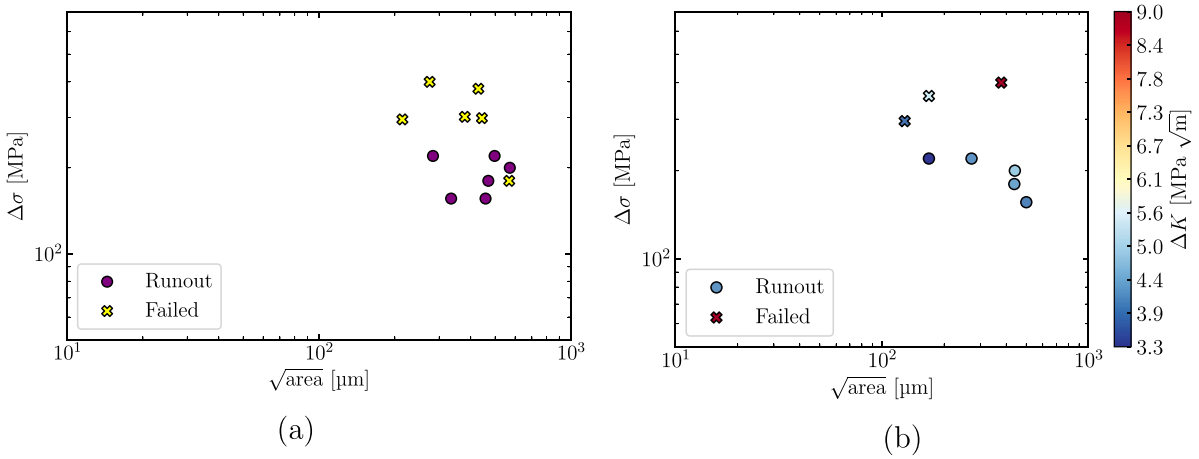

Fig. 2. (a) CT dataset (b) Fractography dataset.

(Eq. (10)) was applied to compute Y and the corresponding ΔK. Table 3 reports the outcomes of this investigation. The defect pertaining to the twelfth sample of Table 3 was originally categorised as sub-surface defect, i.e. $Y = 0.5$. However, EH curve should be referred to a unique class of defect [13]. Maintaining the same ΔK, the equivalent $\sqrt{\text{area}} = 440.0$ µm was computed by assigning $Y = 0.65$ to this defect.

Fig. 2(a) shows the CT dataset given in Table 2, where purple circles and yellow cross markers indicates runout and failed samples, respectively. Similarly, Fig. 2(b) portrays $\sqrt{\text{area}}$ and $\Delta\sigma$ acquired by fractography. Therein, markers are coloured according to the associated ΔK whose value can be read from the rightmost colour bar.

3.2. El Haddad's curve of the fractography dataset

The EH curve is considered to build the physical constraint of the B-PGNN. Such curve is a semi-empirical law that establishes the fatigue endurance limit of metallic alloys referred to a prescribed runout threshold $\mathcal{T}$. Under the hypothesis of LEFM, assuming crack-like defect approximation, and $\sqrt{\text{area}}$ as the defect's characteristic length, the analytical expression of the EH curve turns out

to be [13,71]:

$$\mathcal{E}: \Delta\sigma = \Delta\sigma_w \sqrt{\frac{\sqrt{\text{area}_0}}{\sqrt{\text{area}_0} + \sqrt{\text{area}}}} \tag{11}$$

where $\Delta\sigma_w$ is the fatigue endurance limit of a defect-free specimen, and $\sqrt{\text{area}_0}$ is the so-called EH critical length:

$$\sqrt{\text{area}_0} = \frac{1}{\pi}\left(\frac{\Delta K_{th,lc}}{Y\Delta\sigma_w}\right)^2 \tag{12}$$

where, in turns, $\Delta K_{th,lc}$ is the fatigue crack growth threshold for long cracks.

Given $\Delta K_{th,lc}$ and $\Delta\sigma_w$, the associated EH curve partitions the $\sqrt{\text{area}} - \Delta\sigma$ plane into the region of propagating cracks and non-propagating cracks, above and beneath the curve respectively. Considering a fatigued sample represented by $\mathbf{x}_i = \left[\sqrt{\text{area}_i} \quad \Delta\sigma_i\right]$, the EH curve allows assessing whether pre-existing crack would propagate from a defect when a cyclic load is applied. Specifically, if $\mathbf{x}_i$ falls above the EH curve, the associated specimen is meant to fail. Conversely, if $\mathbf{x}_i$ lays beneath the curve, the specimen is expected to runout. In terms of ML, the EH curve intrinsically defines a dichotomous classification problem where it acts as the decision boundary separating two distinct classes, i.e. runout and failed samples. Consequently, the identification of the EH parameters was carried out using the Maximum a Posterior (MAP) approach comprehensively described in Ref. [49] and briefly summarised herein. The fractographic dataset (Table 3), formally stated as:

$$\mathcal{D}_H = \{(\mathbf{x}_i, \mathcal{F}_i) : \mathbf{x}_i = \left[\sqrt{\text{area}_i} \quad \Delta\sigma_i\right], i = 1,2,3,8,9,10,12\} \tag{13}$$

was used to build the corresponding Bernoulli likelihood, in which $\mathcal{F}_i$ is the ground-truth class computed according to Table 1 and $\mathcal{T} = 2 \cdot 10^6$ as follows:

$$\mathcal{F}_i = \begin{cases} 0 & \text{if } N \geq \mathcal{T} \\ 1 & \text{if } N < \mathcal{T} \end{cases} \tag{14}$$

where 0 and 1 stand for runout and failed, respectively. Whilst the predicted class associated to $\mathbf{x}_i$ is computed by modelling the EH curve via Logistic Regression. Results from the literature were used to inform independent priors $\mathbb{P}[\Delta K_{th,lc}] = \mathcal{N}(4.9, 1.6^2)\,\text{MPa}\sqrt{\text{m}}$ and $\mathbb{P}[\Delta\sigma_w] = \mathcal{N}(330.7, 10.4^2)\,\text{MPa}$ for the EH parameters [72–76]. MAP was then pursued to compute the corresponding marginal posterior distributions $\mathbb{P}[\Delta K_{th,lc}|\mathcal{D}_H]$, and $\mathbb{P}[\Delta\sigma_w|\mathcal{D}_H]$, whose expected values $\Delta\hat{K}_{th,lc}$ and $\Delta\hat{\sigma}_w$ are the EH parameters sought. The EH curve referred to these values will be denoted as $\hat{\mathcal{E}}$.

3.3. Learning El Haddad's curve

The first step necessary for the application of the B-PGNN framework for the present problem aims at encoding the EH curve into the prior of the BNN prior. Nevertheless, while BNNs are flexible models that can be used to tightly approximate any smooth function, they are characterised by a non-linear relationship between the distribution placed on the weights and the resulting functional form of their output. Therefore, the EH curve cannot analytically be encoded. Nevertheless, as highlighted in the following, a method for accurate encoding of the prior can be designed through a combination of synthetic data generation, learning, and posterior tempering by relying on the concept of catalytic priors [66,67].

In the specific problem analysed herein, the set of problem descriptors considered thus far is initially extended. In fact, the application of ML allows for considering features whose relationship with the predictor are already well-understood physically, but also descriptors that potentially hold complementary information. Specifically, beside $\sqrt{\text{area}}$ and already considered in the EH curve, the vector representing the BNN input, $\mathbf{x}_i$, is expanded as:

$$\mathbf{x}'_i = \left[\sqrt{\text{area}_i} \quad d_i \quad S_i \quad \Delta\sigma_i\right] \tag{15}$$

Intuitively, the feature $\sqrt{\text{area}}$ allows the B-PGNN to account for the extension of the defects, whereas the combination of $\sqrt{\text{area}}$ and d (Eq. (8)) indirectly encode the influence of the defect's thickness. Additionally, S (Eq. (7)) was selected as a shape parameter since it introduces the functional dependence on three-dimensional morphological traits. Specifically, S can allow for spheroidal defects (e.g. gas pores) to be distinguished from those being more crack-like (e.g. lack-of-fusion) when $S \to 1$ and $S \to 0$, respectively. Notice that h was not included in the model since Murakami's criterion (Eq. (10)) categorises all the instances of Table 2 as surface defects. Thanks to the flexibility of the present framework, any other available descriptors relevant to the problem can be potentially included in $\mathbf{x}'_i$.

To encode the EH curve in the BNN the catalytic prior framework [66,67], a synthetic dataset is generated such that it encapsulates the behaviour of the EH curve in a discretised fashion. In order to so, a uniform grid over the entries of $\mathbf{x}_i$ is defined – this step only affects $\sqrt{\text{area}_i}$ and $\Delta\sigma_i$. Whilst the additional descriptors specific to the BNN are sampled from a Gaussian distribution with mean and variance set according to the experimental data listed in Table 2:

$$\left[d_i \quad S_i\right] \sim \mathcal{N}(\boldsymbol{\mu} = \left[320 \quad 0.25\right], \boldsymbol{\Sigma} = \text{diag} = (80^2, 0.05^2)) \tag{16}$$

With the resulting samples a synthetic dataset is built as follows:

$$\mathcal{D}_S = \{(\mathbf{x}'_i, \mathcal{F}_i) : \mathbf{x}'_i = \left[\sqrt{\text{area}_i} \quad d_i \quad S_i \quad \Delta\sigma_i\right], i = 1, 2, \dots, \mathsf{M}\} \tag{17}$$

where $\mathcal{F}_i$ depends only on the EH input descriptors.

In short, the catalytic prior is learnt through the BNN from the synthetic dataset $\mathcal{D}_S$. Formally, a standard Gaussian distribution is initially placed over the weight, $\mathbb{P}[\boldsymbol{\theta}|\mathcal{F}]$ so that the catalytic prior is retrieved from a straightforward application of the Bayesian formula:

$$\mathbb{P}[\boldsymbol{\theta}|\mathcal{D}_S, \mathcal{F}] = \frac{\mathbb{P}[\mathcal{D}_S|\boldsymbol{\theta}, \mathcal{F}]^{\tau}\, \mathbb{P}[\boldsymbol{\theta}|\mathcal{F}]}{\mathbb{P}[\mathcal{D}_S|\mathcal{F}]} \tag{18}$$

which is approximated using VI and the implementation is carried out through *Pyro* [77]. Differently from the standard Bayes' theorem (Eq. (4)), Eq. (18) implements an additional parameter τ, called *temperature* [69]. In the current application, τ balances the relative weight between the importance given to the physics, and that given to the observed dataset. Specifically, τ is chosen as suggested in Ref. [66,67] such that $\tau = p/\mathsf{M}$; where $\mathsf{M} = \max\{400, 4p\}$ (Eq. (17),) and p is the number of B-PGNN's parameters. The influence of τ shall be clarified later in regards to the present problem. Furthermore, Eq. (18) is not yet the learning stage of the final B-PGNN, but only its first step encoding the physics information into the BNN model. Before discussing this aspect, however, a Bayesian method to identify a suitable architecture of $\mathcal{F}$ is illustrated.

3.4. Model selection

The design of the BNN prior to reproduce the EH curve has been discussed without referring to any specific architecture $\mathcal{F}$. The present section addresses the issue of selecting the optimal architecture from a given set of configurations following the Bayesian framework. This process is generally referred to as *model selection* [59,78].

Consider the CT dataset given in Table 2, formally:

$$\mathcal{D}_N = \{(\mathbf{x}'_i, \mathcal{F}_i) : \mathbf{x}'_i = \left[\sqrt{\text{area}_i} \mid \mathbf{o}_i \mid \Delta\sigma_i\right], i = 1, 2, \dots, 12\}. \tag{19}$$

where $\mathcal{F}_i$ refers to the ground-truth label obtained by combining the data in Table 1 and Eq. (14). The first step consists in dividing the dataset into a training set, $\mathcal{D}_T$, and a validation one, $\mathcal{D}_V$, which reserves one third of the data for the latter. In addition, a train-test K-fold split is performed thrice, so that each data point is included in the validation set once. This results in the definition of three K-folds pairs which denoted by $\mathcal{D}_T^{(K)}$ and $\mathcal{D}_V^{(K)}$ for $K = 1, 2, 3$. The resulting folds are graphically depicted in Fig. 3.

In order to perform model selection, one is meant to consider a finite dataset of possible configurations. In this instance, fully-connected NN architectures with tanh activation functions are considered [22,37,79]:

$$\mathcal{D}_C = \{\mathcal{F}_{m,n} : m \in \{1, 2\},\ n \in \{16, 32, 64\}\}, \tag{20}$$

where m is the number of hidden layers L, whereas n denotes the neurons belonging to the first hidden layer N_1. If $m = 2$, then $N_2 = N_1/2$ neurons are assigned to the second hidden layer. In any case, the dimension of the input vector $\mathbf{x}'_i$ automatically determines the size of the input layer.

In a Bayesian setting, model selection is performed by selecting the specific architecture that maximises the model evidence for each specific fold K:

$$\mathbb{P}[\mathcal{D}_T^{(K)}|\mathcal{F}_{m,n}] = \int_{\boldsymbol{\theta}} \mathbb{P}[\mathcal{D}_T^{(K)}|\boldsymbol{\theta}, \mathcal{F}_{m,n}]\mathbb{P}[\boldsymbol{\theta}|\mathcal{F}_{m,n}]d\boldsymbol{\theta} \tag{21}$$

Notice that while the integral is in general analytically intractable, it can be numerically approximated [59,78]. Finally, the optimal architecture for each K-fold is selected as:

$$\mathcal{F}^* = \max_{\mathcal{F}_{m,n} \in \mathcal{D}_C;\ K \in \{1,2,3\}} \mathbb{P}[\mathcal{D}_T^{(K)}|\mathcal{F}_{m,n}] \tag{22}$$

3.5. Training on CT data

The final stage of the learning entails the computation of the posterior of the B-PGNN for each optimal architecture and prior designed over the EH curve.

In particular, given the catalytic prior $\mathbb{P}[\boldsymbol{\theta}|\mathcal{D}_S, \mathcal{F}]$ of Eq. (18), the optimal model architecture $\mathcal{F}^*$ is selected as explained in the previous section. The likelihood function over the fold training set, $\mathcal{D}_T^{(K)}$, is the computed and used to evaluate the posterior of the B-PGNN according to Eq. (4). The resulting posterior is approximated using HMC. In this instance, n.8 Markov chains having n.100 samples of $\boldsymbol{\theta}$ randomly explore the parameter space, whereas n.200 samples are dedicated to sample the posterior once the Markov's chains converge. The implementation of HMC was conducted utilising, again, *Pyro* [77]. The resulting posterior distribution $\mathbb{P}[\boldsymbol{\theta}|\mathcal{D}_T^{(K)}, \mathcal{F}^*]$ is finally employed to make predictions as per Eq. (6).

The reader could find the computational framework outlined thus far concisely presented in Appendix A.

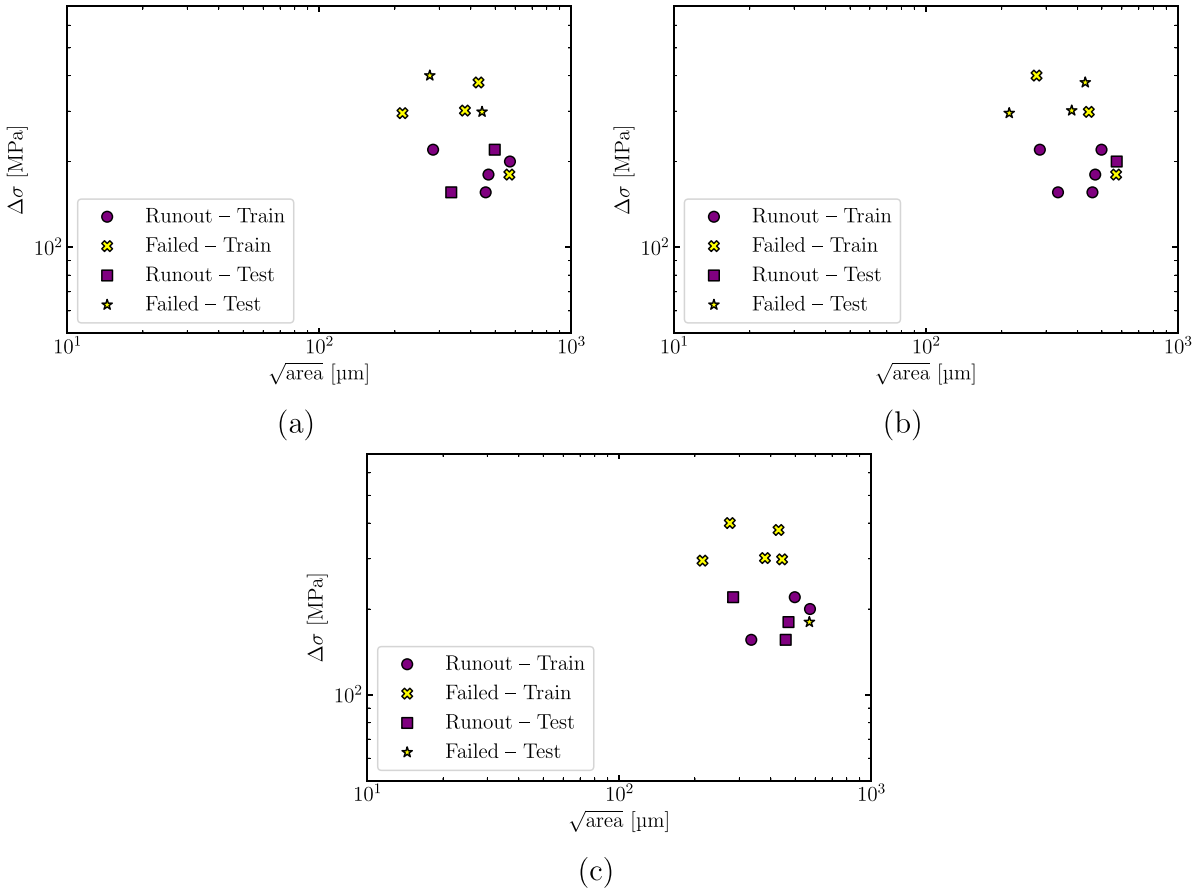

Fig. 3. K-folds adopted to conduct model selection.

4. Result and discussion

4.1. Identified EH curve

The application of MAP provided the expected values of the EH parameters $\hat{\Delta K_{th,lc}} = 6.6\,\text{MPa}\sqrt{\text{m}}$ and $\hat{\Delta\sigma_w} = 349.2\,\text{MPa}$, which univocally identify the EH curve through Eq. (11)–(12). Fig. 4 displays $\Delta\sigma$ alongside $\sqrt{\text{area}}$, and the identified EH curve $\hat{\mathcal{E}}$. A visual examination indicates $\hat{\mathcal{E}}$ to be correctly located at an intermediate position between failed and runout specimens, thus partitioning the dataset $\mathcal{D}_H$, precisely. This result, therefore, substantiates the judicious selection of the adopted prior distributions, i.e. $\mathbb{P}[\Delta K_{th,lc}]$ and $\mathbb{P}[\Delta\sigma_w]$.

4.2. Functional prior of the selected architectures

The implementation of model selection and the guidelines in Ref. [66,67] appointed $\mathcal{F}_{1,16}$ as the optimal architecture for each K-fold $\mathcal{D}_T^{(K)}$. Specifically, $\mathcal{F}_{1,16}$ possess n.1 hidden layer with n.16 neurons totalising $p = 114$ parameters. Correspondingly, this strategy automatically determined the number of training points, i.e. $\mathsf{M} = 484$, required to form the synthetic dataset $\mathcal{D}_S^{(K)}$ (Eq. (17)). Alongside, the value of the temperature parameter turned out be $\tau = 0.236$. The section of $\mathcal{D}_S^{(K)}\ \forall\, K = 1,2,3$ – which is identical for each K-fold – taken on $\sqrt{\text{area}} - \Delta\sigma$ plane is portrayed in Fig. 5. Therein, runout and failed samples of $\mathcal{D}_S^{(K)}$ are denoted by blue and red circle dots, respectively, whereas the solid black line is $\hat{\mathcal{E}}$. It is worth remarking that the descriptors not shown in Fig. 5 follow the normal distribution defined in Eq. (16).

VI was applied on three distinct instances of $\mathcal{F}_{1,16}$ to compute the related the variational approximation of the catalytic prior $\mathbb{P}[\boldsymbol{\theta}|\mathcal{D}_S^{(K)}|\mathcal{F}_{1,16}]\ \forall\, K = 1,2,3$. To qualitatively assess the buoyancy of this stage, Fig. 6 presents the contours of the predictive posterior in terms of the expected value $\mathbb{E}[\mathcal{F}_i]$ and uncertainty $\sqrt{\mathbb{V}[\mathcal{F}_i]}$ of the forecast class $\mathcal{F}_i$. Each figure also depicts failed and runout specimens belonging to the training and test set, i.e. $\mathcal{D}_T^{(K)}$ and $\mathcal{D}_V^{(K)}\ \forall\, K = 1,2,3$, for the sake of convenience. The combination of these contours can be interpreted as the probabilistic fatigue endurance limit of the examined batch of samples. Apart from

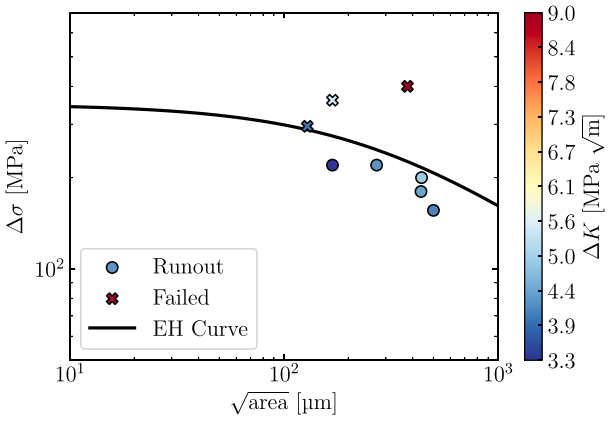

Fig. 4. Graphical representation of the dataset $\mathcal{D}_H$ (Table 3) along with the identified EH curve $\hat{\mathcal{E}}$.

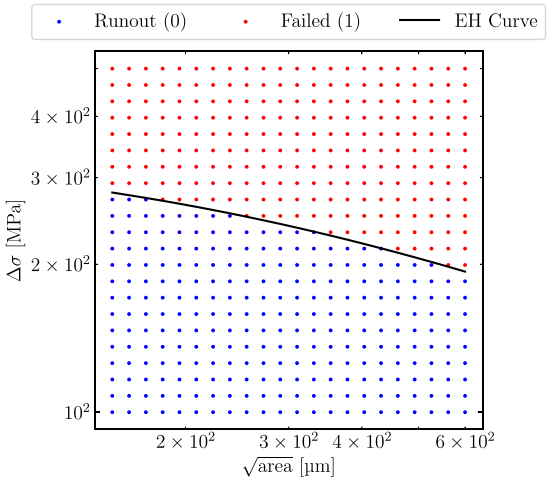

Fig. 5. Section of $\mathcal{D}_S^{(K)}$ taken on $\sqrt{\text{area}} - \Delta\sigma$ plane. This section is identical for each K-fold, whereas the hidden descriptors obey to the distribution of Eq. (16).

modest oscillations ensuing from the random hidden descriptors, the contours bear a close resemblance to one another. A graphical inspection reveals that $\mathcal{F}_{1,16}$ satisfactorily surrogates the EH curve as the contour lines of the predictive posterior globally track the functional form of $\hat{\mathcal{E}}$. Nevertheless, a substantial broadening of the contour lines of $\mathbb{E}[\mathcal{F}_i]$ and a general increase of $\sqrt{\mathbb{V}[\mathcal{F}_i]}$ can be observed along $\hat{\mathcal{E}}$ for approximately $\sqrt{\text{area}} < 150$ MPa and $\sqrt{\text{area}} > 600$ MPa. Therein, $\mathcal{F}_{1,16}$ supposedly extrapolates more than it would do across the sub-domain of the plane where the synthetic training points are concentrated, i.e. $[150, 600] \times [100, 500]$. In contrast, $\mathcal{F}_{1,16}$ achieve greater performance across the interior of this region as the contour lines of $\mathbb{E}[\mathcal{F}_i]$ tightly surround $\hat{\mathcal{E}}$ while showing relatively lower levels of uncertainty.

4.3. Assessing B-PGNN predictions

Each $\mathcal{F}_{1,16}$ was subsequently trained on $\mathcal{D}_T^{(K)}$ through HMC upon prescribing the functional prior $\mathbb{P}[\boldsymbol{\theta}|\mathcal{D}_S^{(K)}|\mathcal{F}_{1,16}]\ \forall\, K = 1, 2, 3$. As a result of the training, the final posterior distribution $\mathbb{P}[\boldsymbol{\theta}|\mathcal{D}_T^{(K)}, \mathcal{H}_{1,16}]$ was computed. Fig. 7 illustrates the contours of $\mathbb{E}[\mathcal{F}_i]$ and $\sqrt{\mathbb{V}[\mathcal{F}_i]}$ of the predictive posterior of each $\mathcal{F}_{1,16}$. For each examined K-fold, the contours ostensibly retain the trend seen in Fig. 6. This finding demonstrates that each B-PGNN preserved the physical knowledge assimilated during VI. Interestingly, the contours attempt to accommodate the conformation of the training datasets. As concerns K-folds n.1, this effect is barely perceptible in Fig. 6(a) since the arrangement of the training points already seem to concur well with the underlying phenomenological law. Nonetheless, the B-PGNN becomes more confident about its predictions in the neighbouring regions of the CT training data. Therein the uncertainty is reduced thanks to the additional training information ensued from CT data, as it can be noticed in Fig. 7(b). The adaptation of the contours to the CT training data is more evident in regards to K-folds n.2. The group five of runouts in $\mathcal{D}_T^{(2)}$ appears as prevailing so that the contours of $\mathbb{E}[\mathcal{F}_i]$ and $\sqrt{\mathbb{V}[\mathcal{F}_i]}$ are shifted downwards on the rightmost portion of the plot (Fig. 7(c)–(d)). Similarly to K-fold n.1, the uncertainty diminishes around the CT training data, see Fig. 7(d). With particular regard to K-fold n.3, the predominant

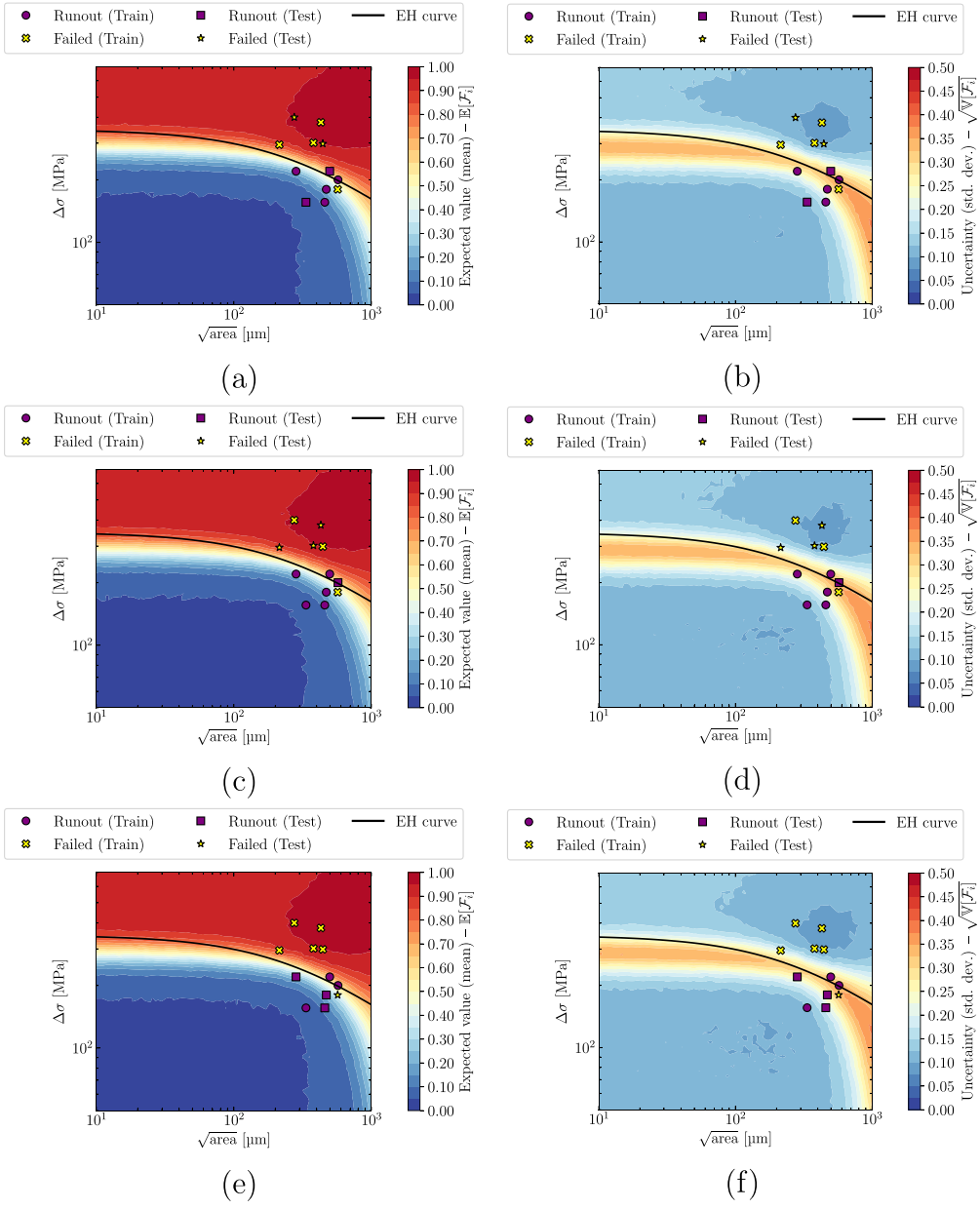

Fig. 6. Contours of the catalytic prior for $D_s^{(K)}\ \forall K = 1, 2, 3$ obtained through VI (a)–(c)-(e) Expected value $\mathbb{E}[\mathcal{F}_i]$. (b)–(d)-(f) Uncertainty $\sqrt{\mathbb{V}[\mathcal{F}_i]}$. The contours are grouped row-wise with respect to the K-folds. (a)–(b) $K = 1$. (c)–(d) $K = 2$. (e)–(f) $K = 3$.

presence of four failed training specimens above $\hat{\mathcal{E}}$ drastically pushes the contours upwards, see Fig. 7(d). Intriguingly, the peculiar collocation of the CT training points suffices to reduce the uncertainty over the entire failed side of the contours.

Box & whisker plots are presented in Fig. 8 to quantitatively assess the obtained predictions. The box spans the interquartile ranges, whereas the whiskers decidedly cover 95% confidence interval. Besides training and test points, the figure reports the median as a short black horizontal line, whilst the expected value of the predictions are denoted as blue triangle markers. The samples are sorted as per Table 2. Except for limited variations, the B-PGNNs achieve similar predictions for samples 1–9. Indeed, this predictions satisfactorily match the experimental expectation for both the training and test datasets. By contrast, little inconsistency is observed with regard to specimens 10–12. These are closely located to $\hat{\mathcal{E}}$ where $\mathbb{E}[\mathcal{F}_i]$ attains values about 0.5 and $\sqrt{\mathbb{V}[\mathcal{F}_i]}$ is relatively high. Therefore, the B-PGNNs cannot exactly distinguish which class the samples belong to. Much attention should be devoted to the

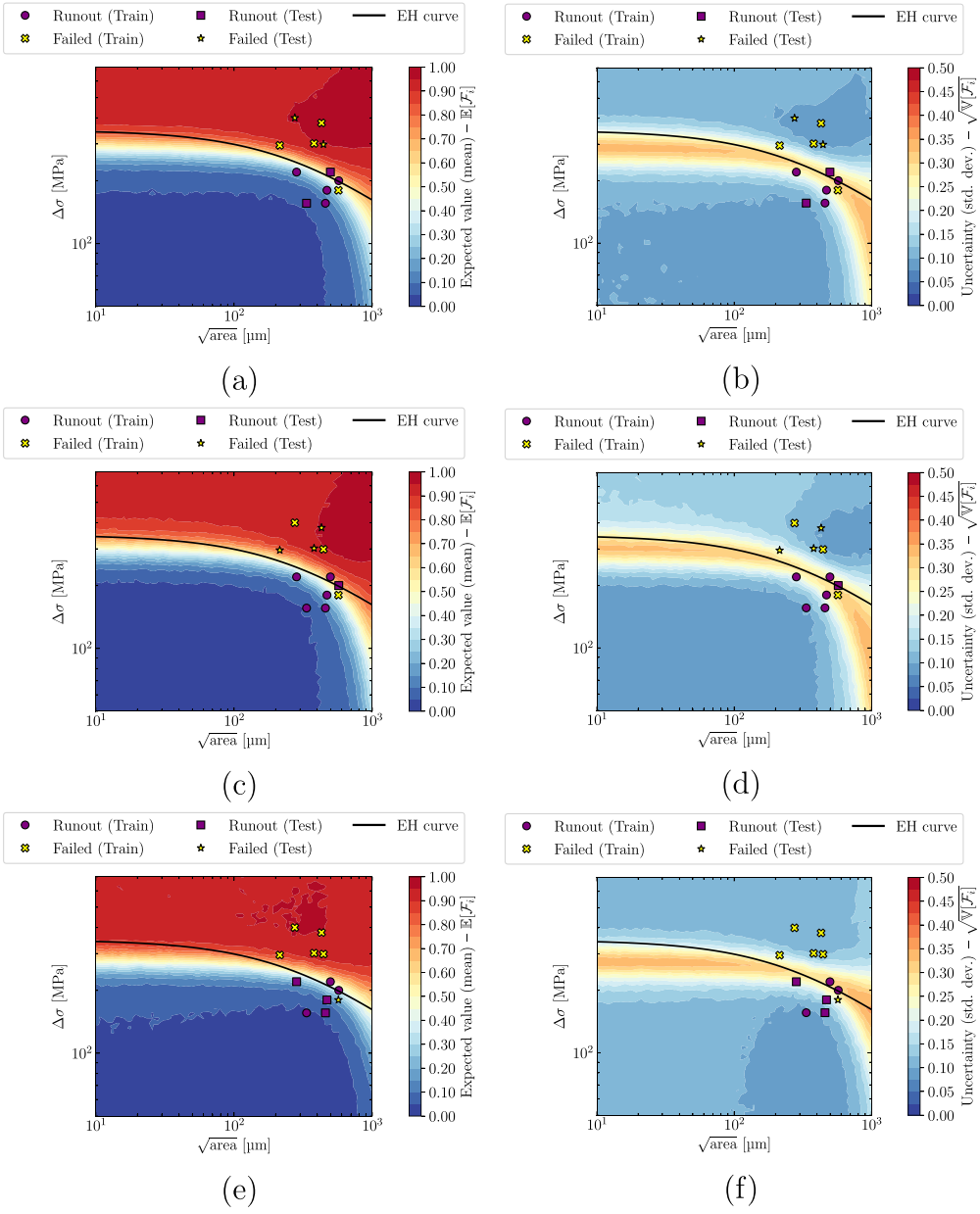

Fig. 7. Contours of the predictive posterior obtained by training $\mathcal{F}_{1,16}$ on $D_T^{(K)}$ $\forall K = 1, 2, 3$ through HMC (a)–(c)-(e) Expected value $\mathbb{E}[F_i]$. (b)–(d)-(f) Uncertainty $\sqrt{\mathbb{V}[F_i]}$. The contours are grouped row-wise with respect to the K-folds. (a)–(b) $K = 1$. (c)–(d) $K = 2$. (e)–(f) $K = 3$.

eleventh sample of the third K-fold (Fig. 7(c)). In this instance, let $\mathbf{x}'_{11}$ be its representative point. Contrary to expectations, the B-PGNN probabilistically classify $\mathbf{x}'_{11}$ as a runout. The apparent lack of matching can attributed to the pathological location of this sample. Focusing on the sole prior knowledge (Fig. 6(e)), $\mathbf{x}'_{11}$ is positioned beneath $\hat{\mathcal{E}}$, where runouts are supposed to lay in. Further, the sample is surrounded by runouts training points which not only prompt the B-PGNN to classify $\mathbf{x}'_{11}$ as runout, but also make the B-PGNN more confident. Certainly, further experimental data surrounding $\mathbf{x}'_{11}$ can compensate for this little inaccuracy. In conclusion, $\mathbf{x}'_{11}$ should essentially be treated as an outlier. Conversely, regarding K-fold n.1 and n.2, $\mathbf{x}'_{11}$ acts as a training point, and it allows one to highlight an interesting property of the B-PGNN. Specifically, the B-PGNN recognise $\mathbf{x}'_{11}$ not complying with the EH semi-empirical law. Consequently, since the B-PGNN becomes unsure about handling this exception, it increases the uncertainty around $\mathbf{x}'_{11}$ to compensate for this apparent mismatch. Therefore, the B-PGNN classifies $\mathbf{x}'_{11}$ with higher uncertainty, and this valuable

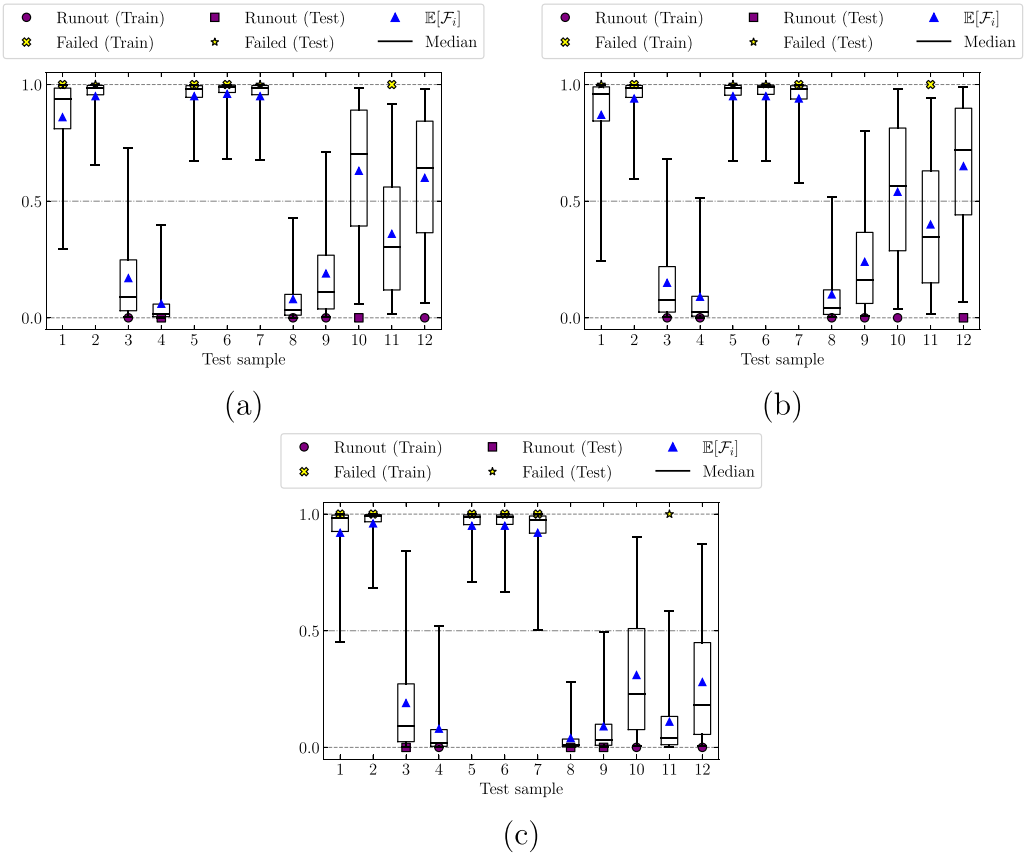

Fig. 8. Box-plots for each K-Fold. The predictions are provided by the B-PGNN after HMC training which exploited the functional prior (a) $K = 1$ (b) $K = 2$. (c) $K = 3$.

information would not have been appreciated with frequentist training, or by training without a physics-guided prior. Although this performance is not ideal, overall, the robustness of the B-PGNNs across the examined K-fold is verified, given the limited number of processed samples. It is worth emphasising that the examined sample are positioned nearby the $\hat{\mathcal{E}}$, where considerable uncertainty is present. Nevertheless, in order to ensure sufficiently reliable parts, engineering design against fatigue failure requires samples to be located sufficiently distant from $\hat{\mathcal{E}}$. To this end, the performance of the B-PGNNs is probed in such regions upon generating an additional synthetic dataset, see Appendix B for further details.

It is worth briefly commenting on the function of τ (Eq. (18)) across the different stages of the training. Specifically, τ intervenes as factor weighting the influence of the functional prior, i.e. $\mathbb{P}[\boldsymbol{\theta}|\mathcal{D}_S^{(K)}, \mathcal{F}_{m,n}]$, and the likelihood ensued from $\mathcal{D}_T^{(K)}$ involved in HMC, i.e. $\mathbb{P}[\mathcal{D}_T^{(K)}|\boldsymbol{\theta}, \mathcal{F}_{m,n}]$. Hence, τ balances the contribution of the physical model and the training data from the CT dataset. The reader could refer to Appendix C for additional details on this.

In order to demonstrate the capabilities of the B-PGNN over the BNN counterpart having the same architecture, HMC was repeated without prescribing the catalytic prior. As concerns the implementation, VI was foregone, and HMC pursued with $\tau = 1$ and a non-informative prior over the parameters. Therefore, this configuration completely neglects the physical knowledge that the catalytic prior brought about earlier. For the sake of brevity, the contours of the predictive posterior are reported in Appendix D. In this case, the contours of $\mathbb{E}[\mathcal{F}_i]$ qualitatively capture the configuration of each dataset, but they do not follow the functional shape of the EH curve. Examining Fig. D.14(a), however, one can claim little similarity the contour in Figs. 7(a) and 7(c). Again, this is fortuitously due to the intrinsic distribution of the training points. Nevertheless, the quantitative predictions are far from being adequate.

Further evidence is provided by the box-plots in Fig. 9 whose box and whiskers span, again, the interquartile range and the 95% confidence interval, respectively. A graphical inspection reveals that the B-PGNN yields more consistent predictions except for the specimens located in the vicinity of the EH which may inherit higher uncertainty from the catalytic prior (see Fig. 6). Apart from these peculiar specimens, the B-PGNN's predictions considerably approach the ground-truth more than the BNN does. In fact, BNN's $\mathbb{E}[\mathcal{F}_i]$ appears to oscillate just within [0.3, 0.6] – considerably deviating from the ground truth value. Moreover, the larger interaquartile range and confidence intervals prevent one from inferring precise information about the predicted class. Since the BNN may provide predictions significantly differing from the actual value, a prospective practitioner would pursue more conservative

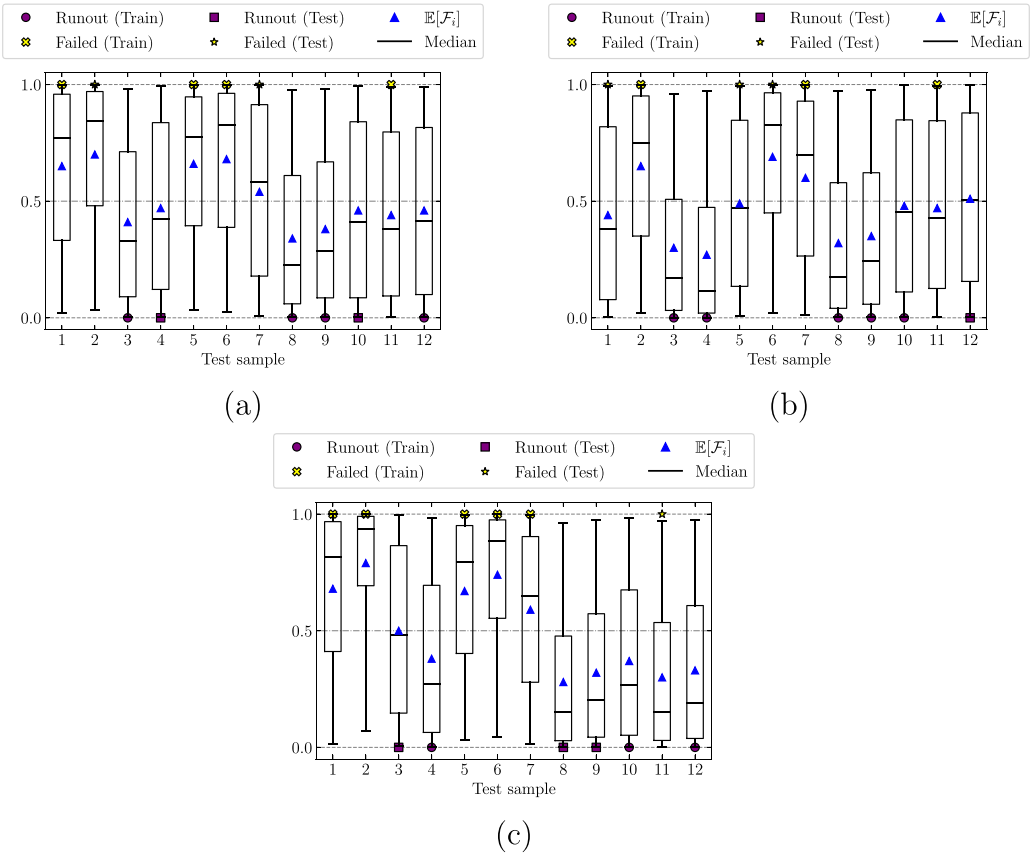

Fig. 9. The predictions provided by the BNN after HMC training without prescribing the functional prior (a) $K = 1$ (b) $K = 2$. (c) $K = 3$.

approaches to tolerate this higher uncertainty in the predictions. Whilst, a more performance-oriented can be adopted by exploiting the superior accuracy of the B-PGNN.

Unlike the classical EH model which exclusively concentrates on $\sqrt{\text{area}}$ and $\Delta\sigma$, the obtained B-PGNNs allow for unveiling potential latent correlations between $\mathcal{F}_i$ and the additional defect descriptors. This can provide insights into phenomena governing fatigue failures. The features were considered in pairs and permuted to study all the possible planes of the input domain, other than $\Delta\sigma - \sqrt{\text{area}}$ already discussed. This investigation was carried out with regard to the third K-fold ($\mathcal{D}_T^{(3)}$) only, for the sake of brevity. The analysis showed positive correlations between $\sqrt{\text{area}}$ and d, $\sqrt{\text{area}}$ and S, and $\Delta\sigma$ and d, whereas negative correlation can be observed between $\Delta\sigma$ and d. On the other hand, no evident relationships connect d and S. Further details on this are reported in Appendix E

5. Conclusions

The present research has showcased a B-PGNN framework to probabilistically forecast whether metallic defect-laden materials experience fatigue failure when subjected to uniaxial fatigue loads. A rigorous Bayesian framework was developed to train the B-PGNNs by inferring a prior knowledge incoming from the data-associated semi-empirical El Haddad curve following a previously proposed procedure. The training culminates in the introduction of experimental evidence from CT data to account for a set of defect descriptors. A selection technique based on model evidence was illustrated to effectively select the most appropriate NN architecture. This approach ensures a full Bayesian treatment of the problem and eliminates the user's arbitrariness on choice NN structure, i.e. layers and neurons.

To test this approach, a literature dataset of SLM AlSi10Mg specimens was considered as a case-study. A K-fold split was employed to assess the robustness of the predictions offered by the developed method. Additionally, it was seen that the B-PGNN outperformed the non-informed BNN counterpart whose training did not involve the prescription of the prior. The tested case-study confirmed that out-of-distribution experimental data might affect the accuracy of the predictions – in extremely small datasets – however the results shown herein are more than satisfactory.

Based on the considered case-study, the developed B-PGNN model allowed for the exploration of potential latent correlations between the prediction and the input descriptors.

The proposed B-PGNN framework makes the most of advanced computational tools and fracture mechanics concepts to establish an unprecedentedly accurate probabilistic predictive model – even for scarce experimental datasets – to efficiently support the design against fatigue failure of defect-laden materials.

CRediT authorship contribution statement

Alessandro Tognan: Conceptualization, Methodology, Investigation, Validation, Data curation, Software, Validation, Writing – original draft. **Andrea Patanè:** Methodology, Validation, Writing – review & editing, Writing – original draft. **Luca Laurenti:** Methodology, Validation, Writing – review & editing, Writing – original draft. **Enrico Salvati:** Conceptualization, Methodology, Investigation, Validation, Writing – review & editing, Writing – original draft, Supervision, Funding acquisition.

Declaration of competing interest

The authors declare that they have no known competing financial interests or personal relationships that could have appeared to influence the work reported in this paper.

Data availability

Data will be made available on request.

Acknowledgements

This work has been supported by the project "CONCERTO – Multiscale modelling/characterisation and fabrication of nanocomposite ceramics with improved toughness" funded by the MUR Progetti di Ricerca di Rilevante Interesse Nazionale (PRIN) Bando 2020 – grant 2020BN5ZW9.

Appendix A. Computational algorithm

Algorithm 1 Computational algorithm for the B-PGNN of the present study.

— EH curve —
Require: Dataset from fractography $\mathcal{D}_H$ ▷ Eq. (13)
Require: Priors for EH parameters $\mathbb{P}[\Delta K_{th,lc}]$ and $\mathbb{P}[\Delta\sigma_w]$
Perform MAP ▷ Ref. [49]
Compute $\mathbb{P}[\Delta K_{th,lc}|\mathcal{D}_H]$ and $\mathbb{P}[\Delta\sigma_w|\mathcal{D}_H]$
Compute EH curve of $\mathcal{D}_H$
— EH catalytic Prior & Model Selection —
Require: EH curve of $\mathcal{D}_H$
Require: Dataset $\mathcal{D}_N$ ▷ Eq.(19)
Require: K-fold split of $\mathcal{D}_N$, i.e. $\mathcal{D}_T^{(K)}$ and $\mathcal{D}_V^{(K)}$
Require: NN architectures $\mathcal{F}_{m,n}$ ▷ Eq. (20)
for $m \in \{1,2\}$ **do**
  for $n \in \{16,32,64\}$ **do**
    Generate synthetic Dataset $\mathcal{D}_S$ ▷ Eq. (17)
    Learn the Catalytic prior through VI
    for $K \in \{1,2,3\}$ **do**
      Compute the evidence of $\mathcal{F}_{m,n}$ on $\mathcal{D}_T^{(K)}$ ▷ Eq.(21)
    end for
  end for
end for
Select the optimal architectures $\mathcal{F}^*$ for each K-fold
— Training on CT data —
Require: K-folds of $\mathcal{D}_N$, i.e. $\mathcal{D}_T^{(K)}$ and $\mathcal{D}_V^{(K)}$
Require: Optimal architectures $\mathcal{F}^*$
for Each optimal architecture **do**
  Prescribe the catalytic prior over θ
  Train B-PGNN through HMC on $\mathcal{D}_T^{(K)}$
  Make predictions ▷ Eq. (6)
end for

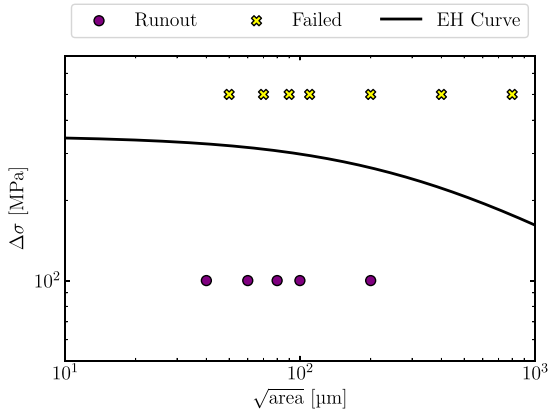

Fig. B.10. Synthetic dataset generated to probe the predictions of the B-PGNN far away from $\hat{\mathcal{E}}$.

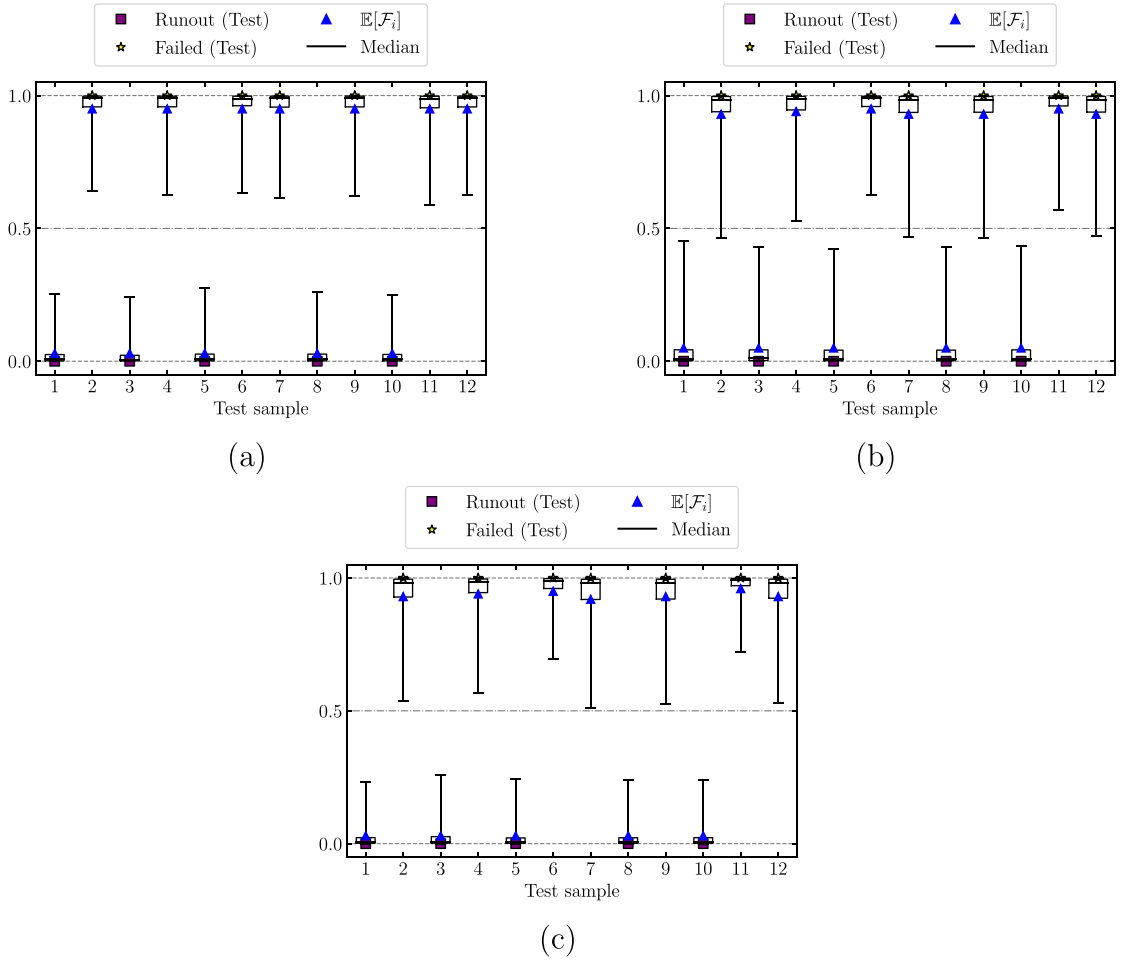

Fig. B.11. Box-plot for the predictions of D_P (a) $K = 1$ (b) $K = 2$. (c) $K = 3$.

Appendix B. Performance of the B-PGNN for engineering practice

The synthetic dataset in Fig. B.10 is generated to assess the predictive capabilities of the B-PGNNs for engineering design against fatigue failure. This dataset will be named as D_P in the following. The dataset is characterised by points remotely located with respect to $\hat{\mathcal{E}}$. Each point belonging to D_P is assumed to possess $d = 320\,\mu\text{m}$ and $S = 0.25$, in agreement with the mean values of the

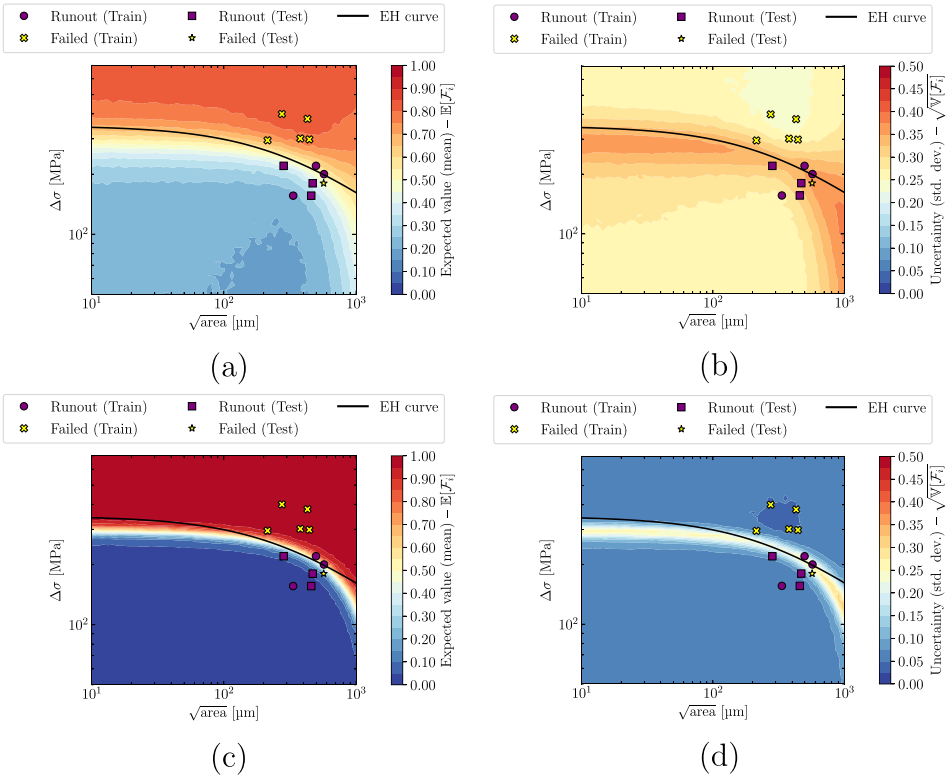

Fig. C.12. Contours of the predictive posterior obtained by training $\mathcal{F}_{1,16}$ on $\mathcal{D}_S^{(3)}$ through VI. (a)–(c) Expected value $\mathbb{E}[F_i]$. (b)–(d) Uncertainty $\sqrt{\mathbb{V}[F_i]}$. The contours are grouped row-wise with respect to τ. (a)–(b) τ_{min}. (c)–(d) τ_{max}.

distribution in Eq. (16). Accordingly, the box & whisker plot in Fig. B.11 gives the associated predictions. Therein, the samples are sorted by $\sqrt{\text{area}}$ as in Fig. B.10. The box-plot clearly demonstrates that the B-PGNN attains accurate predictions on $\mathcal{D}_P$ and proves the suitability of the conceived approach to designing against fatigue failure.

Appendix C. Influence of the temperature τ

This section is briefly presented to expand the discussion about the function of τ across the stages of the training VI and HMC. As far as the extreme instances of τ are concerned, if τ conceptually approaches zero, the physical side of the B-PGNN dominates the posterior. In contrast, if τ becomes increasingly larger, the contribution of the functional prior is progressively purged. Lastly, if $\tau = 1$ the prior and the likelihood are equally balanced.

Additionally, to assess the sensitivity of the temperature parameter on the final predictions, τ is drastically amplified, thus giving $\tau_{\text{min}} = 0.2\,\tau$ and $\tau_{\text{min}} = 5\,\tau$. Fig. C.12 summarises the results obtained through VI upon training on the synthetic dataset in terms of the predictive posterior. As concern the former case, the contours seems to approach those pertaining to the mere data-driven strategy as τ_{min} weakens the prior knowledge inherited from the $\hat{\mathcal{E}}$. Conversely, in the latter instance the physical branch of the B-PGNN is strengthened, thus tightening the contours along $\hat{\mathcal{E}}$.

The choice of τ has direct implication for the final predictions, as shown in Fig. C.13. Specifically, the lack of physical knowledge ensuing from τ_{min} broadened both the interquartile ranges and the confidence intervals. Hence, an overall increase of uncertainty is observed. The opposite behaviour is obtained for τ_{max}, which considerably enhances the confidence of the B-PGNN. As concerns Fig. C.13, $\mathbf{x}'_{11}$ seems to be, again, probabilistically classified as a runout, notwithstanding the reduced value of τ. Therefore, in order to include the possibility for $\mathbf{x}'_{11}$ to be a failed samples, one ought to decrease τ further. Nevertheless, this would lead to an unjustified broadening of the interquartile ranges and confidence intervals of the remaining samples. By contrast, the adoption of τ_{max} confirms $\mathbf{x}'_{11}$ to be a runout. This is mathematically reasonable as $\mathbf{x}'_{11}$ would initially belong to the region where the expected value ranges from 0.3 to 0.4. As previously mentioned, $\mathbf{x}'_{11}$ ought to be treated as an outlier so that its predictions needs to be interpreted with caution.

Appendix D. Predictive posterior of the non-guided B-PGNN

The present appendix reports the contour of the expected value (mean) and uncertainty (standard deviation) of the predictions obtained upon HMC without computing the functional prior through VI. Fig. D.14 present the result in the same manner as those in Figs. 6–7.

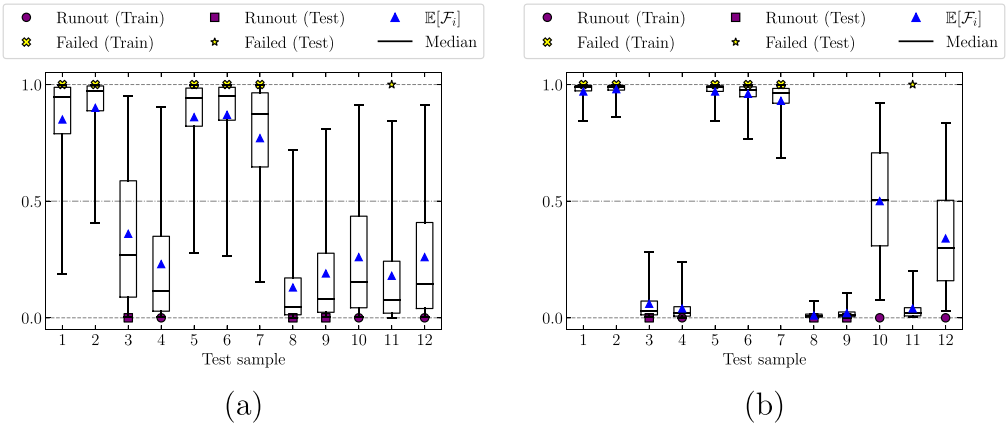

Fig. C.13. The predictions provided by the B-PGNN after HMC (a) τ_{min} (b) τ_{max}.

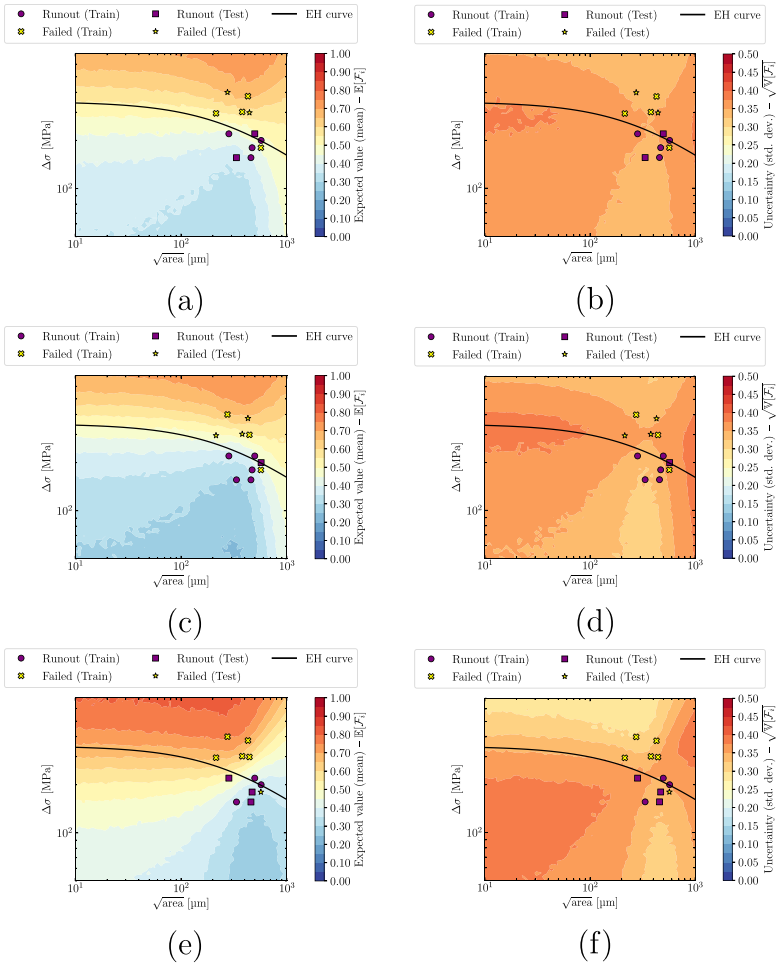

Fig. D.14. Contours of the predictive posterior obtained by training $\mathcal{F}_{1,16}$ on $\mathcal{D}_T^{(K)}$ $\forall\, K = 1, 2, 3$ without prescribing the functional prior. (a)–(c)-(e) Expected value $\mathbb{E}[\mathcal{F}_i]$. (b)–(d)-(f) Uncertainty $\sqrt{\mathbb{V}[\mathcal{F}_i]}$. The contours are grouped row-wise with respect to the K-folds. (a)–(b) $K = 1$. (c)–(d) $K = 2$. (e)–(f) $K = 3$.

Appendix E. Investigation of latent relationships

The present Appendix complements the discussion about the analysis of the correlation between the input features the B-PGNN is meant to process. Fig. E.15 visually summarises the outcomes of this analysis. Particularly, Fig. E.15(a) discloses a positive

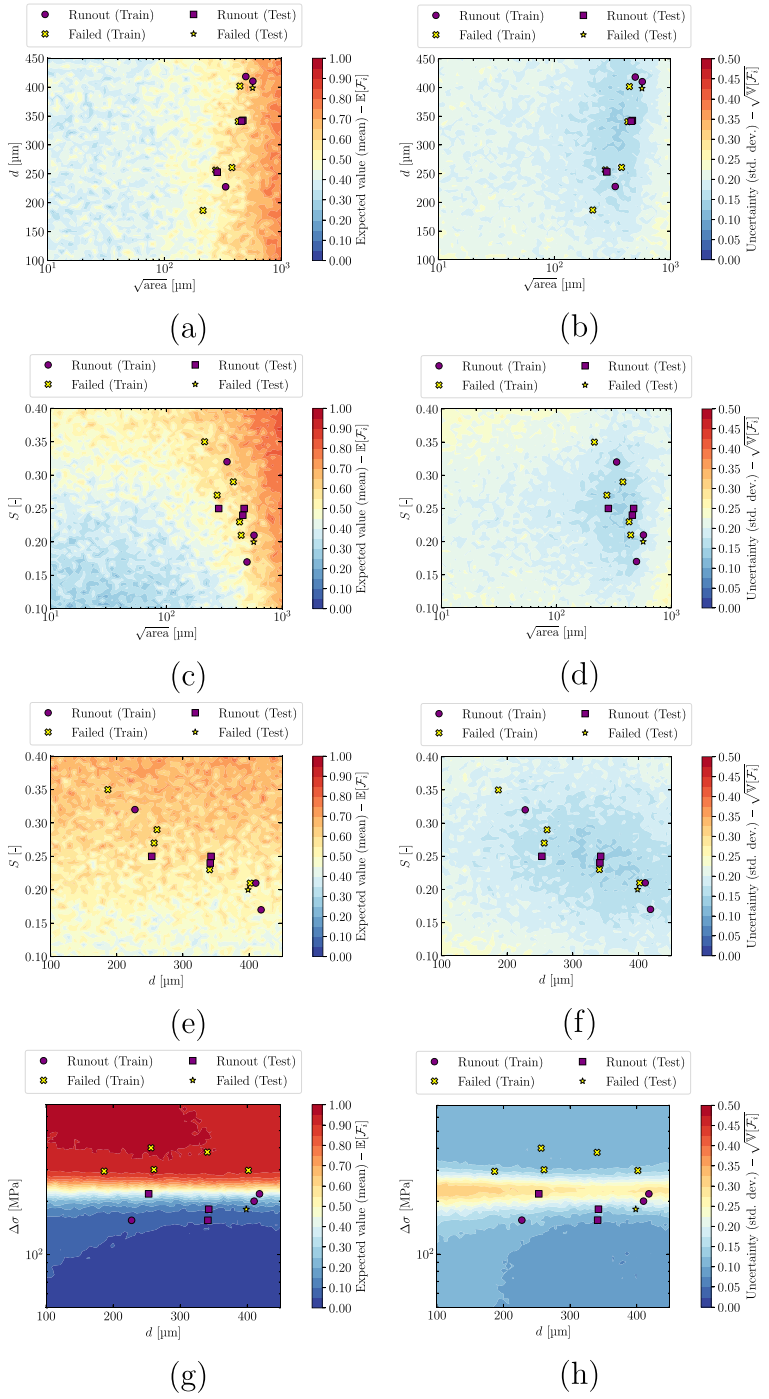

Fig. E.15. Contours of the predictive posterior obtained by training $\mathcal{F}_{1,16}$ on $\mathcal{D}_T^{(3)}$ (the third K-fold) through HMC. Other sections.

correlation between $\sqrt{\text{area}}$ and d, i.e. if these features jointly increase the failure probability increases as well. This appears reasonable since large defects are more likely to trigger fatigue collapse. Unexpectedly, Fig. E.15(b) suggest that $\sqrt{\text{area}}$ and S are positively correlated, which seems, in a word, counterintuitive. In fact, one would suppose that spheroidal defects, i.e. $S \to 1$, yield a minor influence on fatigue failure. Nonetheless, Fig. E.15(b) recalls some of the traits of the EH curve. Presumably, this can be ascribed to the presence of $\sqrt{\text{area}}$ whose behaviour was previously informed by the EH model. However, as concerns Fig. E.15(c), a neat correlation is scarcely distinguishable. Fig. E.15(g) indicates that $\Delta\sigma$ generally controls the predictions, although a mild positive correlation can be recognised. In other words, for increasing d, $\mathbb{E}[\mathcal{F}_i]$ increases, which is in line with theoretical expectations. Still,

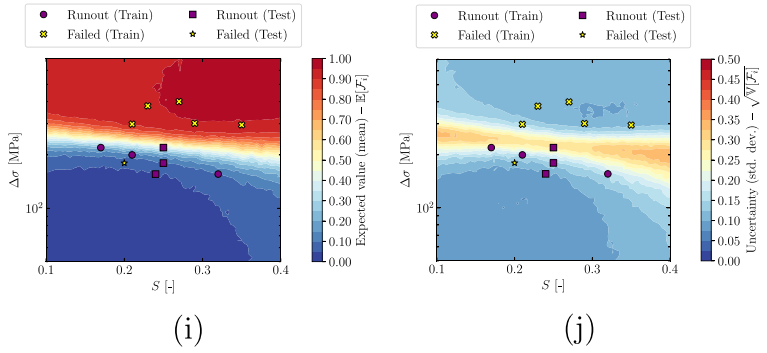

Fig. E.15. (*continued*).

an arguable negative correlation can be noticed in Fig. E.15(i) with regard to S, similarly to that observed in Fig. E.15(c). Therefore, defects having $S \to 0$ ought to possess a crack-like shape, thus more detrimental to fatigue. In any case, the information contained in $\mathcal{D}_T^{(3)}$ allowed the B-PGNN to enhance its predictions. The rightmost panels of Fig. E.15 witnesses diminished uncertainty in the neighbouring region of the training points. It should be mentioned that these sections are partly, or even completely (Fig. E.15(e)–(f)), non-informed by the physical branch. As a result, the patterns that the B-PGNN acquired were inferred from mere data, which corroborates the arrangement of the contours. Potentially, the existing observed discrepancies might be mitigated should further data is provided.

References

[1] G.F. Bocchini, The influences of porosity on the characteristics of sintered materials, in: SAE Transactions, Vol. 95, SAE International, (ISSN: 0096-736X) 1986, pp. 790–805.

[2] Anirudh Sampath Madhvacharyula, Araveeti V. Sai Pavan, Subrahmanyam Gorthi, Srihari Chitral, N. Venkaiah, Degala Venkata Kiran, In situ detection of welding defects: a review, Weld. World (ISSN: 1878-6669) 66 (4) (2022) 611–628, http://dx.doi.org/10.1007/s40194-021-01229-6.

[3] Niloofar Sanaei, Ali Fatemi, Defects in additive manufactured metals and their effect on fatigue performance: A state-of-the-art review, Prog. Mater. Sci. (ISSN: 00796425) 117 (2021) 100724, http://dx.doi.org/10.1016/j.pmatsci.2020.100724.

[4] U. Zerbst, M. Madia, C. Klinger, D. Bettge, Y. Murakami, Defects as a root cause of fatigue failure of metallic components. I: Basic aspects, Eng. Fail. Anal. (ISSN: 13506307) 97 (2019) 777–792, http://dx.doi.org/10.1016/j.engfailanal.2019.01.055.

[5] U. Zerbst, M. Madia, C. Klinger, D. Bettge, Y. Murakami, Defects as a root cause of fatigue failure of metallic components. II: Non-metallic inclusions, Eng. Fail. Anal. (ISSN: 13506307) 98 (2019) 228–239, http://dx.doi.org/10.1016/j.engfailanal.2019.01.054.

[6] U. Zerbst, M. Madia, C. Klinger, D. Bettge, Y. Murakami, Defects as a root cause of fatigue failure of metallic components. III: Cavities, dents, corrosion pits, scratches, Eng. Fail. Anal. (ISSN: 13506307) 97 (2019) 759–776, http://dx.doi.org/10.1016/j.engfailanal.2019.01.034.

[7] Stephen J. Mashl, Hot isostatic pressing of castings, in: Casting, Vol. 12, ASM International, ISBN: 978-1-62708-187-0, 2008, http://dx.doi.org/10.31399/asm.hb.v15.a0005293.

[8] William E. Frazier, Metal additive manufacturing: A review, J. Mater. Eng. Perform. (ISSN: 1059-9495) 23 (6) (2014) 1917–1928, http://dx.doi.org/10.1007/s11665-014-0958-z.

[9] Majid Laleh, Esmaeil Sadeghi, Reynier I. Revilla, Qi Chao, Nima Haghdadi, Anthony E. Hughes, Wei Xu, Iris De Graeve, Ma Qian, Ian Gibson, Mike Y. Tan, Heat treatment for metal additive manufacturing, Prog. Mater. Sci. (ISSN: 0079-6425) 133 (2023) 101051, http://dx.doi.org/10.1016/j.pmatsci.2022.101051.

[10] Yukitaka Murakami, Material defects as the basis of fatigue design, Int. J. Fatigue (ISSN: 01421123) 41 (2012) http://dx.doi.org/10.1016/j.ijfatigue.2011.12.001.

[11] P. Paris, F. Erdogan, A critical analysis of crack propagation laws, J. Basic Eng. (ISSN: 0021-9223) 85 (4) (1963) 528–533, http://dx.doi.org/10.1115/1.3656900.

[12] Y. Murakami, M. Endo, Effects of defects, inclusions and inhomogeneities on fatigue strength, Int. J. Fatigue (ISSN: 0142-1123) 16 (3) (1994) 163–182, http://dx.doi.org/10.1016/0142-1123(94)90001-9.

[13] M.H. El Haddad, K.N. Smith, T.H. Topper, Fatigue crack propagation of short cracks, J. Eng. Mater. Technol. (ISSN: 1528-8889) 101 (1) (1979) 42–46, http://dx.doi.org/10.1115/1.3443647.

[14] Walter Schütz, A history of fatigue, Eng. Fract. Mech. (ISSN: 0013-7944) 54 (2) (1996) 263–300, http://dx.doi.org/10.1016/0013-7944(95)00178-6.

[15] Weicheng Cui, A state-of-the-art review on fatigue life prediction methods for metal structures, J. Mar. Sci. Technol. (ISSN: 09484280) 7 (1) (2002) 43–56, http://dx.doi.org/10.1007/s007730200012.

[16] S. Romano, A. Abel, J. Gumpinger, A.D. Brandão, S. Beretta, Quality control of alsi10mg produced by SLM: Metallography versus CT scans for critical defect size assessment, Addit. Manuf. (ISSN: 22148604) 28 (2019) 394–405, http://dx.doi.org/10.1016/j.addma.2019.05.017.

[17] S. Romano, A. Brückner-Foit, A. Brandão, J. Gumpinger, T. Ghidini, S. Beretta, Fatigue properties of AlSi10Mg obtained by additive manufacturing: Defect-based modelling and prediction of fatigue strength, Eng. Fract. Mech. (ISSN: 00137944) 187 (2018) 165–189, http://dx.doi.org/10.1016/j.engfracmech.2017.11.002.

[18] E. Maire, P.J. Withers, Quantitative X-ray tomography, Int. Mater. Rev. (ISSN: 1743-2804) 59 (1) (2014) 1–43, http://dx.doi.org/10.1179/1743280413Y.0000000023.

[19] Anton du Plessis, Ina Yadroitsava, Igor Yadroitsev, Effects of defects on mechanical properties in metal additive manufacturing: A review focusing on X-ray tomography insights, Mater. Des. (ISSN: 0264-1275) 187 (2020) 108385, http://dx.doi.org/10.1016/j.matdes.2019.108385.

[20] Arun Poudel, Mohammad Salman Yasin, Jiafeng Ye, Jia Liu, Aleksandr Vinel, Shuai Shao, Nima Shamsaei, Feature-based volumetric defect classification in metal additive manufacturing, Nature Commun. (ISSN: 2041-1723) 13 (1) (2022) 6369, http://dx.doi.org/10.1038/s41467-022-34122-x.

[21] Jie Chen, Yongming. Liu, Fatigue modeling using neural networks: A comprehensive review, Fatigue Fract. Eng. Mater. Struct. (ISSN: 1460-2695) 45 (4) (2022) 945–979, http://dx.doi.org/10.1111/ffe.13640.
[22] Lanyi Wang, Shun-Peng Zhu, Changqi Luo, Ding Liao, Qingyuan Wang, Physics-guided machine learning frameworks for fatigue life prediction of AM materials, Int. J. Fatigue (ISSN: 01421123) (2023) 107658, http://dx.doi.org/10.1016/j.ijfatigue.2023.107658.
[23] N.S. Johnson, P.S. Vulimiri, A.C. To, X. Zhang, C.A. Brice, B.B. Kappes, A.P. Stebner, Invited review: Machine learning for materials developments in metals additive manufacturing, Addit. Manuf. (ISSN: 22148604) 36 (2020) 101641, http://dx.doi.org/10.1016/j.addma.2020.101641.
[24] Seunghyun Moon, Ruimin Ma, Ross Attardo, Charles Tomonto, Mark Nordin, Paul Wheelock, Michael Glavicic, Maxwell Layman, Richard Billo, Tengfei Luo, Impact of surface and pore characteristics on fatigue life of laser powder bed fusion Ti–6Al–4V alloy described by neural network models, Sci. Rep. (ISSN: 2045-2322) 11 (1) (2021) 20424, http://dx.doi.org/10.1038/s41598-021-99959-6.
[25] Jun Li, Zhengmao Yang, Guian Qian, Filippo Berto, Machine learning based very-high-cycle fatigue life prediction of Ti-6Al-4V alloy fabricated by selective laser melting, Int. J. Fatigue (ISSN: 01421123) 158 (2022) 106764, http://dx.doi.org/10.1016/j.ijfatigue.2022.106764.
[26] E. Maleki, S. Bagherifard, S.M.J. Razavi, M. Bandini, A. du Plessis, F. Berto, M. Guagliano, On the efficiency of machine learning for fatigue assessment of post-processed additively manufactured AlSi10Mg, Int. J. Fatigue (ISSN: 01421123) 160 (2022) 106841, http://dx.doi.org/10.1016/j.ijfatigue.2022.106841.
[27] Andrea Tridello, Alberto Ciampaglia, Filippo Berto, Davide Salvatore Paolino, Assessment of the critical defect in additive manufacturing components through machine learning algorithms, Appl. Sci. (ISSN: 2076-3417) 13 (7) (2023) 4294, http://dx.doi.org/10.3390/app13074294.
[28] Lei He, Zhilei Wang, Yuki Ogawa, Hiroyuki Akebono, Atsushi Sugeta, Yoshiichirou Hayashi, Machine-learning-based investigation into the effect of defect/inclusion on fatigue behavior in steels, Int. J. Fatigue (ISSN: 01421123) 155 (2022) 106597, http://dx.doi.org/10.1016/j.ijfatigue.2021.106597.
[29] Linwei Dang, Xiaofan He, Dingcheng Tang, Yuhai Li, Tianshuai. Wang, A fatigue life prediction approach for laser-directed energy deposition titanium alloys by using support vector regression based on pore-induced failures, Int. J. Fatigue (ISSN: 01421123) 159 (2022) 106748, http://dx.doi.org/10.1016/j.ijfatigue.2022.106748.
[30] Xin Peng, Shengchuan Wu, Weijian Qian, Jianguang Bao, Yanan Hu, Zhixin Zhan, Guangping Guo, Philip J. Withers, The potency of defects on fatigue of additively manufactured metals, Int. J. Mech. Sci. (ISSN: 00207403) 221 (2022) 107185, http://dx.doi.org/10.1016/j.ijmecsci.2022.107185.
[31] Hongyixi Bao, Shengchuan Wu, Zhengkai Wu, Guozheng Kang, Xin Peng, Philip J. Withers, A machine-learning fatigue life prediction approach of additively manufactured metals, Eng. Fract. Mech. (ISSN: 00137944) 242 (2021) 107508, http://dx.doi.org/10.1016/j.engfracmech.2020.107508.
[32] Anyi Li, Shaharyar Baig, Jia Liu, Shuai Shao, Nima Shamsaei, Defect criticality analysis on fatigue life of L-PBF 17-4 PH stainless steel via machine learning, Int. J. Fatigue (ISSN: 01421123) 163 (2022) 107018, http://dx.doi.org/10.1016/j.ijfatigue.2022.107018.
[33] Y.W. Luo, B. Zhang, X. Feng, Z.M. Song, X.B. Qi, C.P. Li, G.F. Chen, G.P. Zhang, Pore-affected fatigue life scattering and prediction of additively manufactured Inconel 718: An investigation based on miniature specimen testing and machine learning approach, Mater. Sci. Eng. A (ISSN: 09215093) 802 (2021) 140693, http://dx.doi.org/10.1016/j.msea.2020.140693.
[34] Linwei Dang, Xiaofan He, Dingcheng Tang, Bin Wu, Yuhai Li, A fatigue life posterior analysis approach for laser-directed energy deposition Ti-6Al-4V alloy based on pore-induced failures by kernel ridge, Eng. Fract. Mech. (ISSN: 00137944) 289 (2023) 109433, http://dx.doi.org/10.1016/j.engfracmech.2023.109433.
[35] M. Raissi, P. Perdikaris, G.E. Karniadakis, Physics-informed neural networks: A deep learning framework for solving forward and inverse problems involving nonlinear partial differential equations, J. Comput. Phys. (ISSN: 00219991) 378 (2019) 686–707, http://dx.doi.org/10.1016/j.jcp.2018.10.045.
[36] George Em Karniadakis, Ioannis G. Kevrekidis, Lu Lu, Paris Perdikaris, Sifan Wang, Liu Yang, Physics-informed machine learning, Nat. Rev. Phys. (ISSN: 2522-5820) 3 (6) (2021) 422–440, http://dx.doi.org/10.1038/s42254-021-00314-5.
[37] Enrico Salvati, Alessandro Tognan, Luca Laurenti, Marco Pelegatti, Francesco De Bona, A defect-based physics-informed machine learning framework for fatigue finite life prediction in additive manufacturing, Mater. Des. (ISSN: 02641275) 222 (2022) 111089, http://dx.doi.org/10.1016/j.matdes.2022.111089.
[38] Emanuele Avoledo, Alessandro Tognan, Enrico Salvati, Quantification of uncertainty in a defect-based physics-informed neural network for fatigue evaluation and insights on influencing factors, Eng. Fract. Mech. (ISSN: 0013-7944) (2023) 109595, http://dx.doi.org/10.1016/j.engfracmech.2023.109595.
[39] Yukitaka Murakami, Toshio Takagi, Kentaro Wada, Hisao Matsunaga, Essential structure of S-N curve: Prediction of fatigue life and fatigue limit of defective materials and nature of scatter, Int. J. Fatigue (ISSN: 01421123) 146 (2021) 106138, http://dx.doi.org/10.1016/j.ijfatigue.2020.106138.
[40] Davide Leonetti, Johan Maljaars, H.H. (Bert) Snijder, Fitting fatigue test data with a novel S-N curve using frequentist and Bayesian inference, Int. J. Fatigue (ISSN: 0142-1123) 105 (2017) 128–143, http://dx.doi.org/10.1016/j.ijfatigue.2017.08.024.
[41] Daniel Sandberg, Rami Mansour, Mårten Olsson, Fatigue probability assessment including aleatory and epistemic uncertainty with application to gas turbine compressor blades, Int. J. Fatigue (ISSN: 0142-1123) 95 (2017) 132–142, http://dx.doi.org/10.1016/j.ijfatigue.2016.10.001.
[42] L. Patriarca, S. Beretta, S. Foletti, A. Riva, S. Parodi, A probabilistic framework to define the design stress and acceptable defects under combined-cycle fatigue conditions, Eng. Fract. Mech. (ISSN: 00137944) 224 (2020) 106784, http://dx.doi.org/10.1016/j.engfracmech.2019.106784.
[43] Daniel McNeish, On using Bayesian methods to address small sample problems, Struct. Equ. Model. (ISSN: 1532-8007) 23 (5) (2016) 750–773, http://dx.doi.org/10.1080/10705511.2016.1186549.
[44] S. Ghiasi, A. Patane, A. Greco, L. Laurenti, Ep. Scilingo, M. Kwiatkowska, Gaussian processes with physiologically-inspired priors for physical arousal recognition, in: 2020 42nd Annual International Conference of the IEEE Engineering in Medicine & Biology Society, EMBC, Montreal, QC, Canada, July, IEEE, ISBN: 978-1-72811-990-8, 2020, pp. 54–57, http://dx.doi.org/10.1109/EMBC44109.2020.9176437.
[45] Shadi Ghiasi, Andrea Patane, Luca Laurenti, Claudio Gentili, Enzo.Pasquale Scilingo, Alberto Greco, Marta Kwiatkowska, Physiologically-informed Gaussian processes for interpretable modelling of psycho-physiological states, IEEE J. Biomed. Health Inf. (ISSN: 2168-2208) (2022) 1–10, http://dx.doi.org/10.1109/JBHI.2022.3224775.
[46] Radford M. Neal, Bayesian Learning for Neural Networks, Springer New York, New York, NY, 1996, http://dx.doi.org/10.1007/978-1-4612-0745-0.
[47] G Edwards, L.A. Pacheco, A Bayesian method for establishing fatigue design curves, Struct. Saf. (ISSN: 01674730) 2 (1) (1984) 27–38, http://dx.doi.org/10.1016/0167-4730(84)90005-5.
[48] Ivo Babuška, Zaid Sawlan, Marco Scavino, Barna Szabó, Raúl Tempone, Bayesian inference and model comparison for metallic fatigue data, Comput. Methods Appl. Mech. Engrg. (ISSN: 0045-7825) 304 (2016) 171–196, http://dx.doi.org/10.1016/j.cma.2016.02.013.
[49] Alessandro Tognan, Enrico Salvati, Probabilistic defect-based modelling of fatigue strength for incomplete datasets assisted by literature data, Int. J. Fatigue (ISSN: 0142-1123) (2023) 107665, http://dx.doi.org/10.1016/j.ijfatigue.2023.107665.
[50] David J.C. MacKay, Information-based objective functions for active data selection, Neural Comput. (ISSN: 0899-7667) 4 (4) (1992) 590–604, http://dx.doi.org/10.1162/neco.1992.4.4.590.
[51] David J.C. Mackay, Probable networks and plausible predictions — a review of practical Bayesian methods for supervised neural networks, Network: Comput. Neural Syst. (ISSN: 0954-898X) 6 (3) (1995) 469–505.
[52] David J.C. MacKay, Information Theory, Inference, and Learning Algorithms, Cambridge University Press, 2003.
[53] Hyeongwoon Lee, Jongsoo Lee, Neural network prediction of sound quality via domain knowledge-based data augmentation and Bayesian approach with small data sets, Mech. Syst. Signal Process. (ISSN: 08883270) 157 (2021) 107713, http://dx.doi.org/10.1016/j.ymssp.2021.107713.
[54] Hayrettin Okut, Bayesian regularized neural networks for small n big p data, in: Joao Luis Garcia Rosa (Ed.), Artificial Neural Networks - Models and Applications, InTech, ISBN: 978-953-51-2704-8, 2016, http://dx.doi.org/10.5772/63256.
[55] Liu Yang, Xuhui Meng, George Em Karniadakis, B-PINNs: Bayesian physics-informed neural networks for forward and inverse pde problems with noisy data, Journal of Computational Physics (ISSN: 0021-9991) 425 (2021) 109913, http://dx.doi.org/10.1016/j.jcp.2020.109913.

[56] Kevin Linka, Amelie Schäfer, Xuhui Meng, Zongren Zou, George Em Karniadakis, Ellen Kuhl, Bayesian physics informed neural networks for real-world nonlinear dynamical systems, Comput. Methods Appl. Mech. Engrg. (ISSN: 00457825) 402 (2022) 115346, http://dx.doi.org/10.1016/j.cma.2022.115346.
[57] Luning Sun, Jian-Xun Wang, Physics-constrained bayesian neural network for fluid flow reconstruction with sparse and noisy data, Theor. Appl. Mech. Lett. (ISSN: 2095-0349) 10 (3) (2020) 161–169, http://dx.doi.org/10.1016/j.taml.2020.01.031.
[58] Luka Malashkhia, Dehao Liu, Yanglong Lu, Yan Wang, Physics-constrained Bayesian neural network for bias and variance reduction, J. Comput. Inf. Sci. Eng. (ISSN: 1530-9827) 23 (011012) (2022) http://dx.doi.org/10.1115/1.4055924.
[59] David Barber, Bayesian Reasoning and Machine Learning, first ed., Cambridge University Press, ISBN: 978-0-521-51814-7, 2012, http://dx.doi.org/10.1017/CBO9780511804779.
[60] Christopher M. Bishop, Neural Networks for Pattern Recognition, Oxford University Press, 1995.
[61] Radford M. Neal, MCMC using Hamiltonian dynamics, in: Handbook of Markov Chain Monte Carlo, Chapman and Hall/CRC, ISBN: 978-0-429-13850-8, 2011.
[62] Alex Graves, Practical variational inference for neural networks, in: J. Shawe-Taylor, R. Zemel, P. Bartlett, F. Pereira, K.Q. Weinberger (Eds.), Advances in Neural Information Processing Systems, Vol. 24, Curran Associates, Inc., 2011.
[63] David Wingate, Theophane Weber, Automated variational inference in probabilistic programming, 2013, arXiv:1301.1299 [cs, stat].
[64] Rajesh Ranganath, Sean Gerrish, David M. Blei, Black box variational inference, 2013, arXiv:1401.0118 [cs, stat].
[65] Benyamin Ghojogh, Ali Ghodsi, Fakhri Karray, Mark Crowley. Factor Analysis, Probabilistic principal component analysis, variational inference, and variational autoencoder: Tutorial and survey, 2022, arXiv:2101.00734 [cs, stat].
[66] Dongming Huang, Nathan Stein, Donald B. Rubin, S.C. Kou, Catalytic prior distributions with application to generalized linear models, Proc. Natl. Acad. Sci. (ISSN: 1091-6490) 117 (22) (2020) 12004–12010, http://dx.doi.org/10.1073/pnas.1920913117.
[67] Dongming Huang, Feicheng Wang, Donald B. Rubin, S.C. Kou, Catalytic priors: Using synthetic data to specify prior distributions in Bayesian analysis, 2022.
[68] Eric Thomas Nalisnick, On Priors for Bayesian Neural Networks, University of California, Irvine, 2018.
[69] Florian Wenzel, Kevin Roth, Bastiaan S. Veeling, Jakub Świkatkowski, Linh Tran, Stephan Mandt, Jasper Snoek, Tim Salimans, Rodolphe Jenatton, Sebastian Nowozin, 2020, arXiv preprint arXiv:2002.02405.
[70] Yukitaka Murakami, Metal Fatigue: Effects of Small Defects and Nonmetallic Inclusions, Elsevier, 2019.
[71] Uwe Zerbst, Giovanni Bruno, Jean-Yves Buffière, Thomas Wegener, Thomas Niendorf, Tao Wu, Xiang Zhang, Nikolai Kashaev, Giovanni Meneghetti, Nik Hrabe, Mauro Madia, Tiago Werner, Kai Hilgenberg, Martina Koukolíková, Radek Procházka, Jan Džugan, Benjamin Möller, Stefano Beretta, Alexander Evans, Rainer Wagener, Kai Schnabel, Damage tolerant design of additively manufactured metallic components subjected to cyclic loading: State of the art and challenges, Prog. Mater. Sci. (ISSN: 0079-6425) 121 (2021) 100786, http://dx.doi.org/10.1016/j.pmatsci.2021.100786.
[72] S. Romano, L. Patriarca, S. Foletti, S. Beretta, LCF behaviour and a comprehensive life prediction model for AlSi10Mg obtained by SLM, Int. J. Fatigue (ISSN: 01421123) 117 (2018) 47–62, http://dx.doi.org/10.1016/j.ijfatigue.2018.07.030.
[73] S. Beretta, M. Gargourimotlagh, S. Foletti, A. du Plessis, M. Riccio, Fatigue strength assessment of as built AlSi10Mg manufactured by SLM with different build orientations, Int. J. Fatigue (ISSN: 0142-1123) 139 (2020) 105737, http://dx.doi.org/10.1016/j.ijfatigue.2020.105737.
[74] S. Beretta, L. Patriarca, M. Gargourimotlagh, A. Hardaker, D. Brackett, M. Salimian, J. Gumpinger, T. Ghidini, A benchmark activity on the fatigue life assessment of AlSi10Mg components manufactured by L-PBF, Mater. Des. (ISSN: 0264-1275) 218 (2022) 110713, http://dx.doi.org/10.1016/j.matdes.2022.110713.
[75] M. Bonneric, C. Brugger, N. Saintier, A. Castro Moreno, B. Tranchand, Contribution of the introduction of artificial defects by additive manufacturing to the determination of the Kitagawa diagram of Al-Si alloys, Procedia Struct. Integr. (ISSN: 24523216) 38 (2022) 141–148, http://dx.doi.org/10.1016/j.prostr.2022.03.015.
[76] Timothy D. Piette, Robert J. Warren, Anthony G. Spangenberger, Edward J. Hummelt, Diana A. Lados, Microstructure evolution, fatigue crack growth, and ultrasonic fatigue in as-fabricated laser powder bed and conventionally cast Al–10Si-0.4Mg: A mechanistic understanding and integrated flaw-sensitive fatigue design methods, Mater. Sci. Eng. A (ISSN: 0921-5093) 825 (2021) 141892, http://dx.doi.org/10.1016/j.msea.2021.141892.
[77] Eli Bingham, Jonathan P. Chen, Martin Jankowiak, Fritz Obermeyer, Neeraj Pradhan, Theofanis Karaletsos, Rohit Singh, Paul A. Szerlip, Paul Horsfall, Noah D. Goodman, Pyro: Deep universal probabilistic programming, J. Mach. Learn. Res. 20 (2019) 28:1–28:6.
[78] Jie Ding, Vahid Tarokh, Yuhong Yang, Model selection techniques: An overview, IEEE Signal Process. Mag. (ISSN: 1558-0792) 35 (6) (2018) 16–34, http://dx.doi.org/10.1109/MSP.2018.2867638, Conference Name: IEEE Signal Processing Magazine.
[79] Taotao Zhou, Shan Jiang, Te Han, Shun-Peng Zhu, Yinan Cai, A physically consistent framework for fatigue life prediction using probabilistic physics-informed neural network, Int. J. Fatigue (ISSN: 01421123) (2022) 107234, http://dx.doi.org/10.1016/j.ijfatigue.2022.107234.